JGR Atmospheres

RESEARCH ARTICLE
10.1029/2020JD032529

Special Section:
Years of the Maritime Continent

Diurnal Cycle of Precipitation Over the Maritime Continent Under Modulation of MJO: Perspectives From Cloud-Permitting Scale Simulations

Yuntao Wei[1], Zhaoxia Pu[1], and Chidong Zhang[2]

[1]Department of Atmospheric Sciences, University of Utah, Salt Lake City, UT, USA, [2]NOAA Pacific Marine Environmental Laboratory, Seattle, WA, USA

Abstract Cloud-permitting scale (3 km) simulations are made to investigate the diurnal cycle of precipitation (DCP) over the Indo-Pacific Maritime Continent under the modulation of the Madden-Julian Oscillation (MJO), focusing on January–February 2018 during the Years of the Maritime Continent (YMC). Comparisons with satellite precipitation and global reanalysis products show that the simulations reasonably capture main features of diurnal wind and precipitation. The MJO modulates the amplitude, timing, and propagation of the DCP through affecting both large-scale and local circulation and convection. Under local suppressed conditions, much strengthened sea/valley breezes are generally responsible for the enhanced and earlier-triggered (2- to 3-hr lead) DCP over land. Meanwhile, stronger cooling induced by enhanced stratiform rainfall excites well-developed gravity waves spreading outward and upward, accompanied by continuous decreases in low-level temperature and amplified land breezes, which cause stronger and further offshore-propagating DCP. The opposite is true under local active conditions. Modulated by the passing of MJO, the enhanced DCP also displays a systematic shift from the west to the east coasts of large islands, forming a unique dipolar structure in the anomalous island DCP. The DCP exhibits island-dependent characteristics: With topographical elevation, the triggering mechanism of island convection transforms from later penetrating sea breeze fronts over mountain foothills to early-excited valley winds over mountain tops. Steep topography also supports stronger intraseasonal variations of the DCP, which can be well explained by regional variations in land-sea/mountain-valley breezes, terrain lifting, and ambient wind-induced advective and vertical wind shear effects.

Key Points:
- Cloud-permitting simulations demonstrate the roles of land-sea breezes, elevated terrain, valley winds, and gravity waves in diurnal precipitation over the Maritime Continent
- The MJO modulates the amplitude, timing, and propagation of diurnal precipitation through a combination of varying large-scale and local circulations and convection
- The diurnal precipitation cycle under the MJO modulation varies among islands depending on their size and topography

Supporting Information:
- Supporting Information S1

Correspondence to:
Z. Pu,
zhaoxia.pu@utah.edu

Citation:
Wei, Y., Pu, Z., & Zhang, C. (2020). Diurnal cycle of precipitation over the Maritime Continent under modulation of MJO: Perspectives from cloud-permitting scale simulations. *Journal of Geophysical Research: Atmospheres*, *125*, e2020JD032529. https://doi.org/10.1029/2020JD032529

Received 31 JAN 2020
Accepted 20 MAY 2020
Accepted article online 23 MAY 2020

1. Introduction

The Maritime Continent (MC) is the largest archipelago on Earth and features a mixture of islands and oceans centering on the Indo-Pacific Warm Pool (Margono et al., 2014). Tremendous latent heat released from vigorous convective processes over the MC fuels the global atmospheric circulation, which in turn significantly influences local and global weather and climate (e.g., Adames & Wallace, 2014; Jin & Hoskins, 1995; Neale & Slingo, 2003; Qian, 2008; Ramage, 1968; B. Wang & Li, 1994; Yamanaka et al., 2018; Zhang, 2013). Despite the unmatched role of the MC in the weather-climate continuum, most state-of-the-art general circulation models (GCMs) still struggle to accurately simulate small-scale processes, especially the diurnal cycle of precipitation (DCP) and its impacts over the MC, due to their coarse resolution and poor representation of complex land-sea contrast and topography (Baranowski et al., 2019; Qian, 2008; Yang & Slingo, 2001). It is also extremely challenging to accurately predict high-impact weather and climate events in this region (Neena et al., 2014; Seo et al., 2009; S. Wang et al., 2019). Therefore, there is an urgent need to deeply understand the convective characteristics over the MC and their underlying mechanisms, and the key task is to discover the intriguing multiscale interactions across diurnal and longer periods (Chang et al., 2004; McBride, 1998). The DCP and its interactions with large-scale variabilities, for example, the tropical intraseasonal oscillation (TISO, Lau & Waliser, 2012; Zhang, 2005; Xie et al., 2018), is at the heart of the theme of atmospheric convection in the Years of the Maritime Continent (YMC) project (Yoneyama & Zhang, 2020).

Since satellite observations became available in 1979, great progress has been made in understanding the DCP in the tropics, especially its global distribution (e.g., Gentemann et al., 2003; Hendon & Woodberry, 1993; Kikuchi & Wang, 2008; Sakaeda et al., 2017; Taylor, 2012; Yang & Slingo, 2001). Some fundamental characteristics of the DCP have been well documented: For example, large-amplitude DCP tends

to occur exclusively over land and coastal areas, while over the open ocean away from coastlines the DCP is weaker and usually displays some persistent characteristics (Vincent & Lane, 2017). This is very different from the TISO, of which signals over the ocean are much stronger than those over land (e.g., Sobel et al., 2008, 2010). From a statistical point of view (e.g., Kikuchi & Wang, 2008; Vincent & Lane, 2017; Yang & Slingo, 2001), the maximum DCP over land and coastal areas is usually observed from late afternoon to evening, while oceanic precipitation peaks from mid night to early morning. The DCP also shows evident offshore and/or inland propagation. These statistical features of the DCP may also be modulated by transient disturbances (such as tropical cyclones, equatorial waves, and cold surges) and large-scale variabilities. Moreover, there are also some interesting spatial variations in the timing of the peak DCP over land and the extent and direction of offshore migrating mesoscale convective systems across different land-sea areas. Yang and Slingo (2001), for example, showed that regional variations in the DCP may indicate the effects of complex land-sea and mountain-valley breezes, as well as the life cycle of mesoscale convective systems. They also found variations in the distance at which the island DCP could spread over adjacent oceans, probably induced by gravity waves (GWs) of different depths.

Basic theories and mechanisms have also been advanced to explain the land-sea contrast in the DCP. The land-sea breezes resulted from the distinctive heat capacity and surface conditions of land and sea (Miller et al., 2003) have been extensively used to explain the DCP. For example, the strong DCP over islands is caused predominantly by sea-breeze convergence, reinforced by valley winds and further amplified by cumulus merger processes (e.g., Birch et al., 2015; Qian, 2008; Simpson et al., 1993; Yang & Slingo, 2001). For coastal and oceanic regions, however, the situation is much more complicated, and there may be several mechanisms responsible for the offshore-propagating behaviors of the DCP: (1) GWs excited by nighttime radiative cooling over elevated terrains extend outward and upward, destabilize the offshore atmosphere and contribute to the migration of diurnal precipitation (e.g., Mapes et al., 2003; Warner et al., 2003); (2) same functions of GWs but excited by the evaporative cooling of land precipitation (e.g., Hassim et al., 2016; Love et al., 2011; Vincent & Lane, 2016; Yokoi et al., 2017); (3) gravity (or density) currents, such as land breezes and cold outflows, which trigger new convection via convergence with ambient winds or cold outflows from other islands (e.g., Fujita et al., 2010; Houze et al., 1981; Mori et al., 2004; Wapler & Lane, 2012; Wu et al., 2009); and (4) influences of ambient winds, such as the advection effect (e.g., Ichikawa & Yasunari, 2006, 2008; Yanase et al., 2017) and the vertical wind shear mechanism (e.g., LeMone et al., 1998; Yokoi et al., 2019). With these proposed mechanisms, we still do not know which one is the dominant process and how they vary with different islands in the MC.

As a dominant mode of the TISO, the Madden-Julian Oscillation (MJO) (Madden & Julian, 1971, 1972) initiated from the western Indian Ocean (Matthews, 2008; Wei et al., 2019, 2020) can modulate the behavior of the DCP (e.g., Fujita et al., 2011; Hassim et al., 2016; Ichikawa & Yasunari, 2006, 2008; Kanamori et al., 2013; Lu et al., 2019; Vincent & Lane, 2016, 2018). In general, the amplitude of the island DCP reaches its maximum during a local MJO suppressed period and reaches its minimum in an MJO active period, while the opposite is true for the oceanic DCP (e.g., Birch et al., 2016; Oh et al., 2012; Peatman et al., 2014; Rauniyar & Walsh, 2011; Sakaeda et al., 2017; Vincent & Lane, 2017). However, some studies have shown that the DCP is enhanced in active periods and reduced in suppressed periods of the MJO regardless of the land-sea contrast (e.g., Chen & Houze, 1997; Sui et al., 1997; Tian et al., 2006). There have also been conflicting views regarding the modulation effect of the MJO on the DCP phase (i.e., the timing of the maximum diurnal precipitation). For example, Rauniyar and Walsh (2011) and Sakaeda et al. (2017) both suggested that the peak time of the DCP during active days of the MJO lags that for all days by 2–3 hr, while during suppressed days of the MJO triggering of the DCP is earlier by 2–3 hr than for all days. By contrast, other studies have shown that the DCP phase is not significantly affected by the MJO (e.g., Suzuki, 2009; Tian et al., 2006). Moreover, the proposed mechanisms for the modulation effect of the MJO on the DCP are quite diverse (e.g., Birch et al., 2016; Fujita et al., 2011; Ichikawa & Yasunari, 2006, 2008; Peatman et al., 2014, 2015; Sakaeda et al., 2017).

The above review demonstrates that there are still much uncertainties in our understanding of the processes associated with the triggering and propagation of the DCP as well as their MJO modulation effects over the MC. In addition, most of the previous studies focusing on this topic have considered only very localized areas of the MC and did not systematically investigate island-dependent characteristics in the MJO modulation of

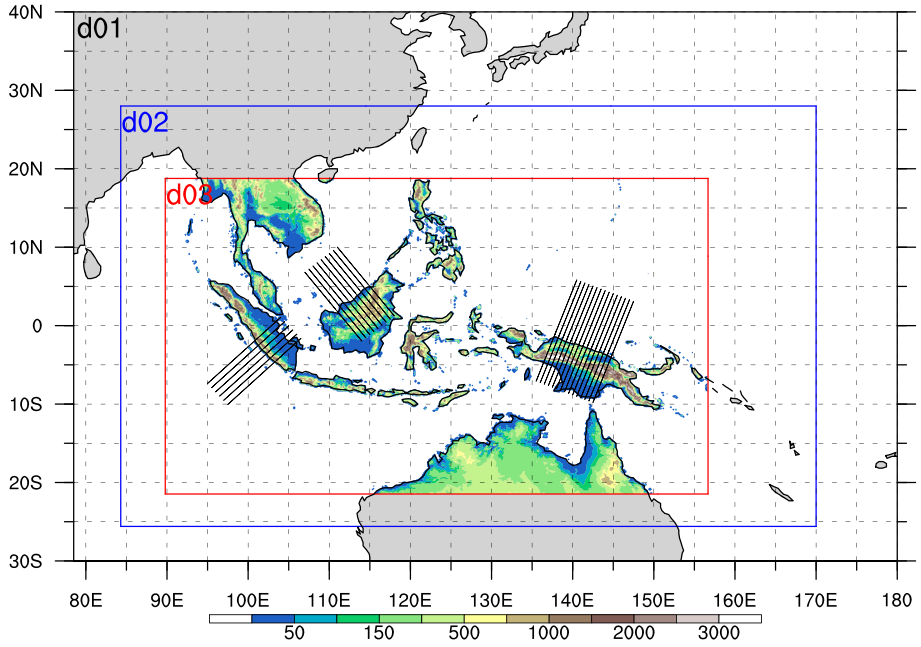

Figure 1. The Model Domain d01 (black), d02 (blue), and d03 (red). Colors in Domain d03 represent the terrain height (m). Black parallel lines in Domain d03 are the transects used to calculate the mean diurnal cycle over the islands of Sumatra, Borneo, and New Guinea and the surrounding ocean.

the DCP. The modulation effect may be very different over different islands because of their sizes, orientations, and terrain heights (e.g., Li & Carbone, 2015; Riley Dellaripa et al., 2019; Wang & Sobel, 2017). Motivated by these uncertainties, we address two key questions in this study. (1) What do the main characteristics of the DCP over the MC vary across different land/sea areas under the influence of the MJO? (2) How different are the dominant mechanisms by which the MJO modulates the DCP over different land/sea areas? We focus on three major islands of the MC: Sumatra, Borneo, and New Guinea (Figure 1). Each island has unique topographic features and geometries, and together, they are a good test bed to study the questions above.

Because the resolution of global reanalysis data is too coarse (~27 km) to resolve the details of the DCP (see supporting information Figure S1 and Text S1), in this study, we used an advanced research version of the Weather Research and Forecasting (WRF) model (Version 4.0) to generate numerical simulations at the cloud-permitting scale (3 km). The modeling domain (Figure 1) covers the entire Indo-Pacific Warm Pool and can be adopted to investigate regional variations in the MJO modulation effect on the DCP. We focused on the period from January to February 2018, during which the strongest MJO event during the YMC in 2017–2019 occurred. The outgoing longwave radiation (OLR)-based MJO index (OMI; Kiladis et al., 2014) is very strong (i.e., greater than one standard deviation) in both months, which allows us to study the DCP throughout the entire life cycle of this MJO event. This is quite different from some previous studies that covered only one part of the MJO life cycle (e.g., Hassim et al., 2016; Vincent & Lane, 2016; Yokoi et al., 2017, 2019). Along this line, we expect to contribute to the broad goals of the YMC theme of atmospheric convection, especially the DCP and its scale interaction with the MJO.

The rest of this paper is arranged as follows. Section 2 introduces the numerical simulations, the data, and methodology used in this study. Section 3 gives an overview of the large-scale background of the MJO event. Section 4 introduces the simulated mean DCP and its variation at different MJO stages, where both the general view and the regional variations are examined. Section 5 explains the mechanisms of MJO modulation from the perspective of both large-scale environmental conditions and local mesoscale variations. The paper concludes with a brief summary of the main findings and a discussion of their broader implications.

2. Model, Data, and Methodology

2.1. WRF Model and Configurations

The advanced research Version 4.0 of the WRF model (Skamarock et al., 2019) is a fully compressible and nonhydrostatic model using the hybrid vertical coordinate system. Three, two-way nesting domains (d01, d01, and d03) were used with horizontal grid spacing of 27, 9, and 3 km, respectively (Figure 1). In the vertical, 32 η levels have been used with the top of the model at 50 hPa. Note that the modeling domains, even the innermost one of 3-km grids, can cover the entire Indo-Pacific warm pool region. Specifically, it starts in the central eastern Indian Ocean (~90°E) to the west and reaches the South Pacific Convergence Zone (~157°E) to the east. The meridional range from 20°S to 20°N is also large enough to cover the decaying scale of equatorial waves and the MJO (Kiladis et al., 2009). A set of well-tested physical parameterization schemes specific for tropical regions were used, including the WSM six-class graupel microphysical scheme, a new Tiedtke cumulus scheme (for d01 and d02 only), the RRTMG longwave and shortwave radiation schemes, the Yonsei University (YSU) planetary boundary layer (PBL) scheme, a unified Noah land-surface model, and the old MM5 surface layer scheme.

We performed WRF simulations from January to February 2018. The numerical simulations were conducted for 30 hr cold started from 0000 UTC every day. The first 6 hr are considered as the spin-up period and are not included in the model diagnostics. The initial and boundary conditions are from the National Centers for Environmental Prediction (NCEP) Final (FNL) data. We refer to this set of simulations as the control simulations or simple the simulations. In order to examine the role of high terrains in influencing the diurnal wind and precipitation, we also performed one additional set of sensitivity experiments focusing on New Guinea during the period of 16–20 January 2018. In these sensitivity experiments, terrain height greater than 600 m was changed to 600 m. These experiments are named "REDUCE_TOPO_RUN." The model configuration and the initial and boundary conditions are all the same as in the control simulations, except the model domain covers a small region surrounding New Guinea.

2.2. Data

Three types of precipitation products have been used to verify and compare with the simulations. They are the Tropical Rainfall Measuring Mission (TRMM) multisatellite precipitation analysis (Huffman et al., 2007) 3B42v7 products at 0.25° × 0.25° and 3-hr resolutions, the Integrated Multi-satellitE Retrievals for Global Precipitation Mission (IMERG) (Huffman et al., 2015) at 0.1° × 0.1° and 0.5-hr resolution, and National Oceanic and Atmospheric Administration (NOAA)'s Climate Prediction Center morphing technique (CMORPH) (Joyce et al., 2004) at a horizontal resolution of 8 km and a time step of 30 min.

The European Centre for Medium-Range Weather Forecasts (ECMWF) Interim reanalysis (ERA-I; Dee et al., 2011) and the newest ERA5 global reanalysis (Copernicus Climate Change Service, C3S, 2017), both at the same spatial resolution of 0.25° × 0.25°, are used for providing large-scale background. The temporal resolution for ERA-I and ERA 5 is different. While ERA-I data are available at 6-hourly, ERA5 data are available hourly.

We also use the gridded daily NOAA OLR with temporal and spatial interpolations (Liebmann & Smith, 1996) to represent convective cloud associated with the MJO. The NOAA OLR is available from 1974 to the present with a spatial resolution of 2.5° × 2.5°. In addition, the daily OMI from January to February 2018 is also used. The OMI is calculated based on the first two empirical orthogonal function (EOF) modes of the 30- to 96-day eastward only OLR between 20°S and 20°N (Kiladis et al., 2014). Compared with the conventional real-time multivariate MJO (RMM) index (Wheeler & Hendon, 2004), which largely depends on upper tropospheric circulation signals (Straub, 2013), the OMI is more suitable to represent convective signals of the MJO.

2.3. Methodology

To assess the fidelity of the WRF model in representing the standard DCP with a period of 24 hr, we use the following equation (Love et al., 2011; Peatman et al., 2014):

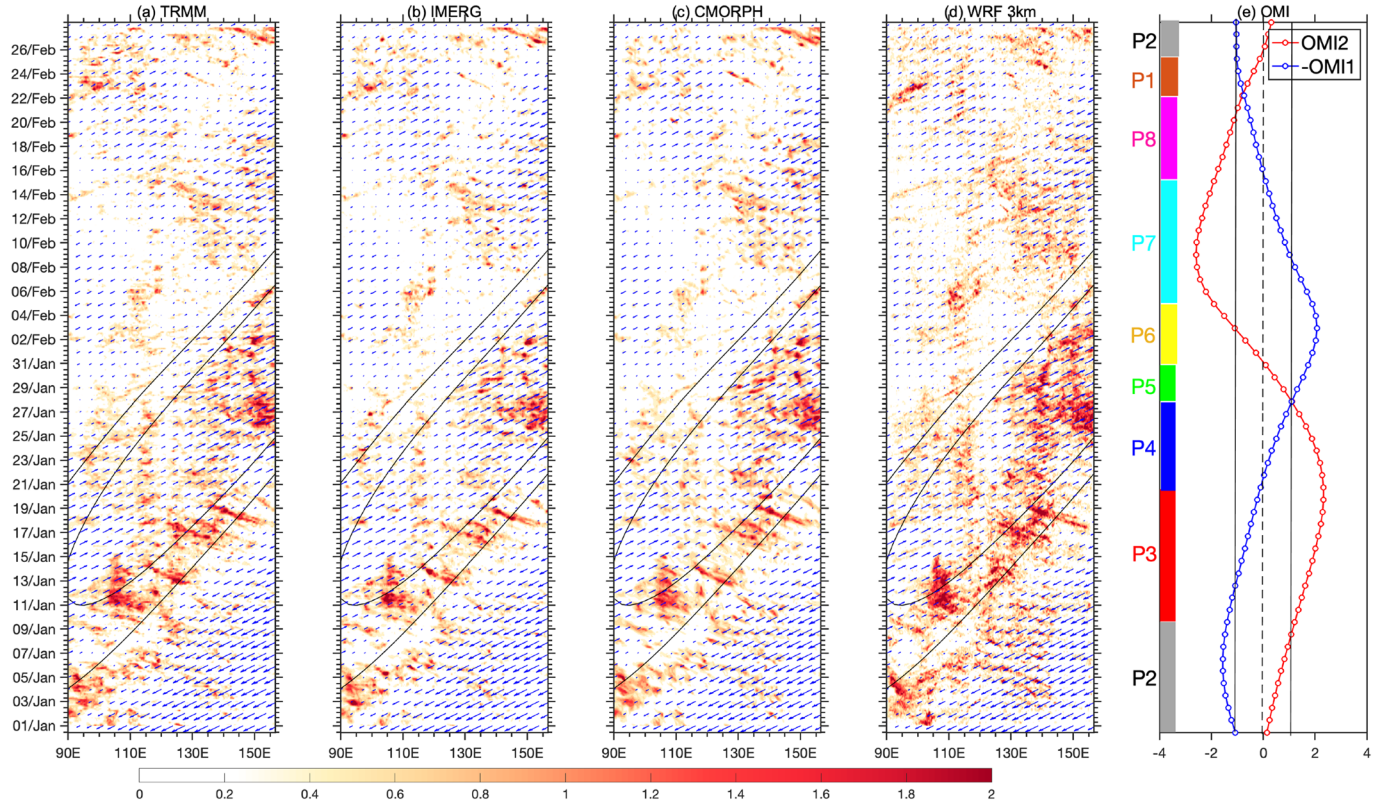

Figure 2. Hovmöller diagrams of 3-hourly precipitation (mm hr^{-1}) averaged over 15°S to 15°N from (a) TRMM, (b) IMERG, (c) CMORPH, and (d) the control simulations. Blue vectors are band-pass-filtered (30- to 90-day) daily mean horizontal wind anomalies (m s^{-1}) at 850 hPa from ERA-I (southerlies upward). Black contours show MJO-filtered OLR anomalies (−10 and −5 W m^{-2}) from NOAA satellite observation. (e) Time series of OMI2 (red) and −OMI1 (blue) with each day marked by a circle. The two vertical solid lines denote the one standard deviations. Color bars highlight eight OMI phases (i.e., P1 to P8).

$$R(t) = R_m + R_d \cos\left[\frac{2\pi}{\tau}(t - Phi)\right], \tag{1}$$

where $R(t)$ is the raw precipitation time series, t the hour of the day, R_m the daily mean precipitation rate, R_d the amplitude of the DCP, Phi the phase of the DCP (the time when $R(t)$ reaches its maximum), and $\tau = 24$ hr. To use Equation 1, the composite 3-hr time series of $R(t)$ should first be calculated. For example, the composite at time i (i = 00, 03, 06, 09, 12, 15, 18, and 21 UTC, respectively) of the day was calculated as the mean from $i - 1$ to $i + 1$. To extract the diurnal variability in the global reanalysis (ERA-I and FNL), we also interpolated their 6-hourly data into 3-hourly data. The local solar time (LST) is converted from UTC according to the local longitude (i.e., LST = UTC + longitude/15). The diurnal anomaly was also diagnosed, which is calculated as the departure from the daily mean.

The 30- to 90-day band-pass filtering using a Lanczos filter with 201 weights was applied to the daily anomalies of satellite-derived OLR and reanalysis data to extract the intraseasonal variability. The daily anomaly is obtained by removing the daily climatology. To display the envelopes associated with the large-scale, eastward propagating MJO, MJO-filtering techniques (Kiladis et al., 2009; Wheeler & Kiladis, 1999) were also used here. For example, the planetary-scale MJO envelope can be obtained using an inverse Fourier transform to retrieve the signals that retain only the Fourier coefficients of eastward propagating Zonal Wavenumbers 1–6 and frequencies from 1/96 to 1/30 cycles per day.

3. Large-Scale Precipitation and the Embedding MJO

Figure 2 shows the Hovmöller diagrams of 3-hr simulated and observed precipitation. The large-scale wave envelope of the MJO derived from the daily observed OLR and the 30- to 90-day filtered horizontal wind

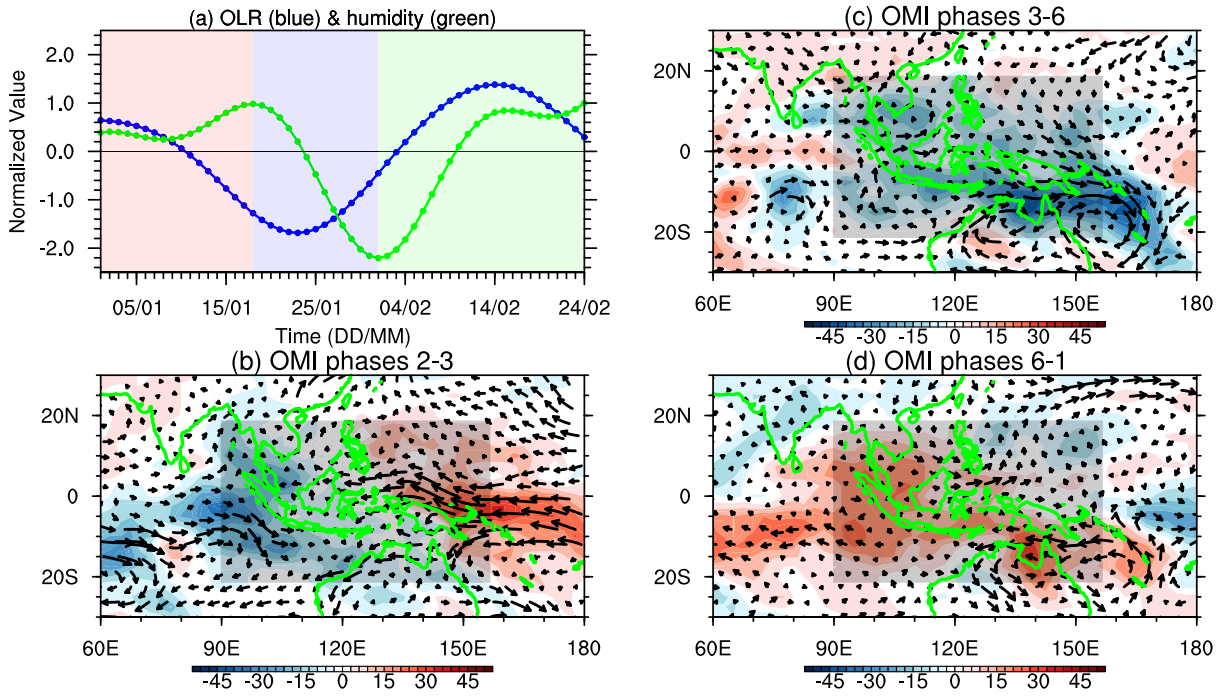

Figure 3. (a) Time evolution of the observed 30- to 90-day filtered OLR (blue) and ERA-I 850-hPa specific humidity (green) anomalies averaged over Domain d03. Both OLR and humidity have been normalized by their perspective one standard deviation. The red, blue, and green backgrounds denote respectively the OMI Phases 2–3, 3–6, and 6–1. (b–d) Averaged maps of the 30- to 90-day filtered OLR and ERA-I 850-hPa wind anomalies at the three MJO stages, respectively. The gray shading represents the Domain d03 shown in Figure 1.

anomalies at 850 hPa from the reanalysis are overlaid. In satellite-derived products (Figures 2a to 2c), high precipitation is mainly embedded in the large-scale envelopes of the MJO. The small-scale characteristics of the precipitation, especially those over the leading edge of the MJO envelope, are dominated by westward propagating signals with a period of roughly two days (Kikuchi & Wang, 2010; Yu et al., 2018). There are strong diurnal variations in precipitation, displaying both eastward and westward propagation and largely depending on the flow direction of intraseasonal zonal wind anomalies. Overall, the control simulations (Figure 2d) can realistically simulate the precipitation as observed by the satellite-derived products, including both large-scale and small-scale signals, albeit with slightly overestimated amplitudes.

To reveal the large-scale background of the precipitation evolution, the MJO event is analyzed. Following Hung and Sui (2018), the MJO life cycle is partitioned into three stages: the MC preconditioning, active, and suppressed stages, according to the d03-averaged, 30- to 90-day band-pass-filtered observed OLR anomalies and specific humidity anomalies from the reanalysis (Figure 3a). The three stages correspond to OMI Phases 2–3, 3–6, and 6–1, respectively (Figure 2e). At the MC preconditioning stage (1–18 January 2018), the atmosphere exhibits a moistening tendency and a transition from positive to negative OLR anomalies. At the MC active stage from 18 January to 1 February 2018, convection reaches its peak, and humidity decays quickly to its minimum as it is consumed by heavy precipitation. At the MC suppressed stage from 2 to 24 February 2018, deep convection begins to decay, and the atmosphere becomes less moist.

Table 1 summarizes the large-scale convective conditions in the OMI phases over d03 and three major islands. For Sumatra and Borneo, OMI Phases 2–3 and 3–6 correspond to the local convection growth and decay conditions, respectively. For New Guinea, however, these two groups of OMI phases are local preconditioning and active conditions. In OMI Phases 6–1, all islands are under local suppressed conditions. Therefore, this method based on d03 alone is able to well capture the local preconditioning (only for New Guinea), active, and suppressed periods of the MJO.

Figures 3b to 3d show composite maps of the 30- to 90-day filtered OLR and 850-hPa wind anomalies in different OMI phases. It is apparent that during OMI Phases 2–3 (Figure 3b), deep convection is located

Table 1
Large-Scale Convection Conditions in Different OMI Phases Over the Model Domain (d03) and Three Major Islands

Time period	OMI phases	Large-scale convective conditions over the areas			
		The model domain (d03)	*Sumatra*	*Borneo*	*New Guinea*
1–18 January 2018	2 and 3	MC preconditioning	Local convection growth	Local convection growth	Local preconditioning
19 January to 1 February 2018	3, 4, 5, and 6	MC active	Local convection decaying	Local convection decaying	Local active
2–24 February 2018	6, 7, and 1	MC suppressed	Local suppressed	Local suppressed	Local suppressed

primarily over the Indian Ocean, while convection over the eastern MC and western Pacific is suppressed. Large-scale easterly anomalies associated with equatorial Kelvin waves dominate over the MC, while large-scale westerly anomalies associated with equatorial Rossby waves are over the Indian Ocean. During OMI Phases 3–6 (Figure 3c), the low-level circulation over the northwest coast of Borneo and northeast coast of New Guinea shifts from easterly to westerly anomalies, and 850-hPa wind over Sumatra becomes much stronger. During OMI Phases 6–1 (Figure 3d), the entire MC region becomes less cloudy and less windy.

4. Mean DCP and its Variation at Different MJO Stages

To understand the DCP variation under MJO influence, we examine the mean DCP and its variation at different MJO stages. As shown in Figure 2, the simulations capture the main features and evolution of precipitation over the MC region. Meanwhile, the spatial and temporal distributions of the precipitation revealed by different satellite data are quite consistent. Considering the similarities of IMERG and CMORPH data products in their spatial and temporal resolutions and also the phases of the DCP derived from them, in the rest of this study, we use averages of IMERG and CMORPH (referred to as "averaged satellite retrieval") to represent the satellite-based precipitation and DCP (section 4). The TRMM data are not included in the averaged satellite retrieval because of the different resolution from IMERG and CMORPH.

4.1. General Features Over the MC Region

Figure 4 shows the three DCP parameters in Equation 1. In the averaged satellite retrievals, large mean precipitation (R_m) occurs over the MC islands and coastal regions, such as the areas over and around Sumatra, Borneo, Java, New Guinea, Timor, the east coast of the Philippines, and the Malay Peninsula (Figure 4a). The spatial distributions of R_m are generally well simulated by the simulations (Figure 4c), even though slightly overestimated. The ratio of R_m between the simulations and satellite retrievals (Figure 4e) reveals that the overestimate of mean precipitation is especially high over steep topography, straits, and along concave coastlines. The overestimation of precipitation is a common outstanding problem in simulated island precipitation using high-resolution models (e.g., Birch et al., 2015; Hassim et al., 2016; Love et al., 2011; Vincent & Lane, 2016).

The satellite retrievals show large DCP amplitudes (R_d) mainly over land and near coastlines (such as Java, Borneo, north coast of Australia, and New Guinea) and very weak oceanic DCP (Figure 4b). This implies that the land precipitation can be attributed to diurnal variability (e.g., Birch et al., 2015; Peatman et al., 2014). The land-sea distribution of R_d observed by the satellite retrievals is generally simulated reasonably well by the WRF model (Figure 4d). However, the simulated DCP amplitudes are too large (almost 2 to 4 times larger than the observed) over the islands, especially over and near their steep topography as shown by the ratio of R_d between the simulations and satellite retrievals (Figure 4e). These large simulation biases over land may imply that the model exaggerates the impacts of land surface processes on precipitation. The DCP is also overestimated over the Gulf of Carpentaria, probably due to the enhanced convergence effect associated with the inward curvature of the coastline (Biasutti et al., 2012; Jiang, 2012).

In the satellite retrievals, there is an evident land-sea contrast in the phase of the DCP (*Phi*), where island rainfall peaks from late afternoon to midnight, and oceanic rainfall generally peaks during early morning (Figure 4g). *Phi* also displays strong dependence on island size. For small islands, the peak time is often earlier than for large islands (Nesbitt & Zipser, 2003; Qian, 2008). In addition, *Phi* shows an increasing trend with increasing distance away from coastlines, reflecting the offshore migration of the DCP. The

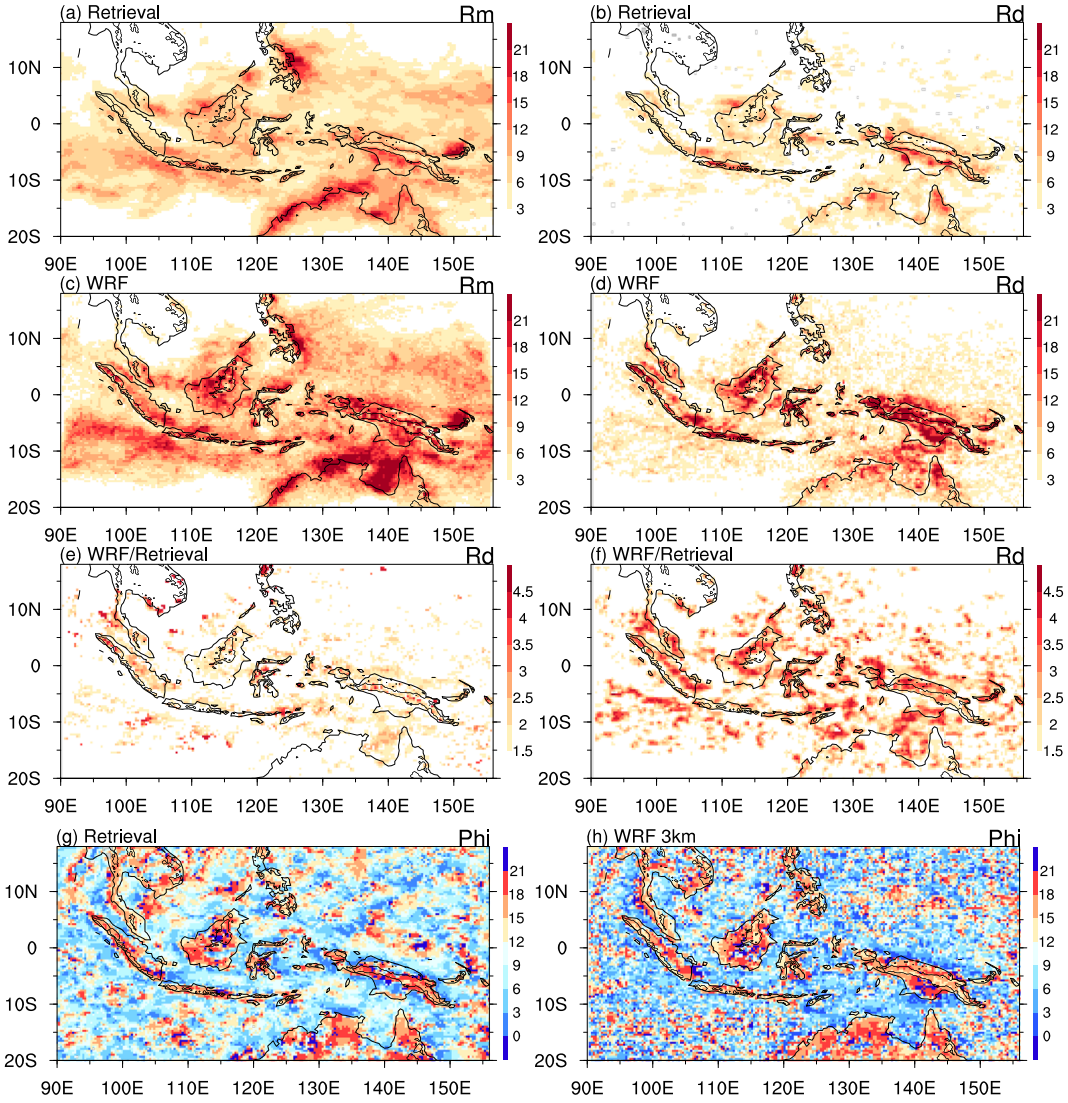

Figure 4. (a) Precipitation rate R_m (mm day^{-1}) and (b) amplitude of the diurnal cycle in precipitation (DCP) R_d derived from the composite of IMERG and CMORPH satellite retrievals. (c and d) Same as (a) and (b) but for WRF simulation. Ratio of (e) R_m and (f) R_d between the simulation and satellite retrievals. Phase of DCP *Phi* derived from (g) the composite of IMERG and CMORPH satellite retrievals and (h) the simulations. All variables were averaged over January to February 2018. Black contours represent the terrain height of 0 (coastlines) and 600 m.

simulations clearly reproduce the land-sea contrast in *Phi* (Figure 4h), although some biases appear over land areas with steep topography, where convection peaks 3–6 hr earlier than in the satellite retrievals. The bias in simulated *Phi*, especially the peak ~6 hr too early over steep topography, has also been reported in many other studies (e.g., Love et al., 2011; Vincent & Lane, 2016, 2017). However, biases of 2- to 3-hr delay in satellite precipitation products as compared to rain gauge data (e.g., Birch et al., 2015; Kikuchi & Wang, 2008; Lu et al., 2019) should partially compensate for the bias in simulated *Phi*.

4.2. DCP Over Sumatra, Borneo, and New Guinea

To have a clearer and more quantitative examination of the regional variation of the DCP, we further examine the DCP over three major islands in the MC: Sumatra, Borneo, and New Guinea. Following previous studies (e.g., Short et al., 2019), we draw a series of parallel lines perpendicular to the coastlines of these islands (Figure 1), along which the phase propagation of the DCP as well as its three key parameters (R_m, R_d, *Phi)* are quantitatively analyzed.

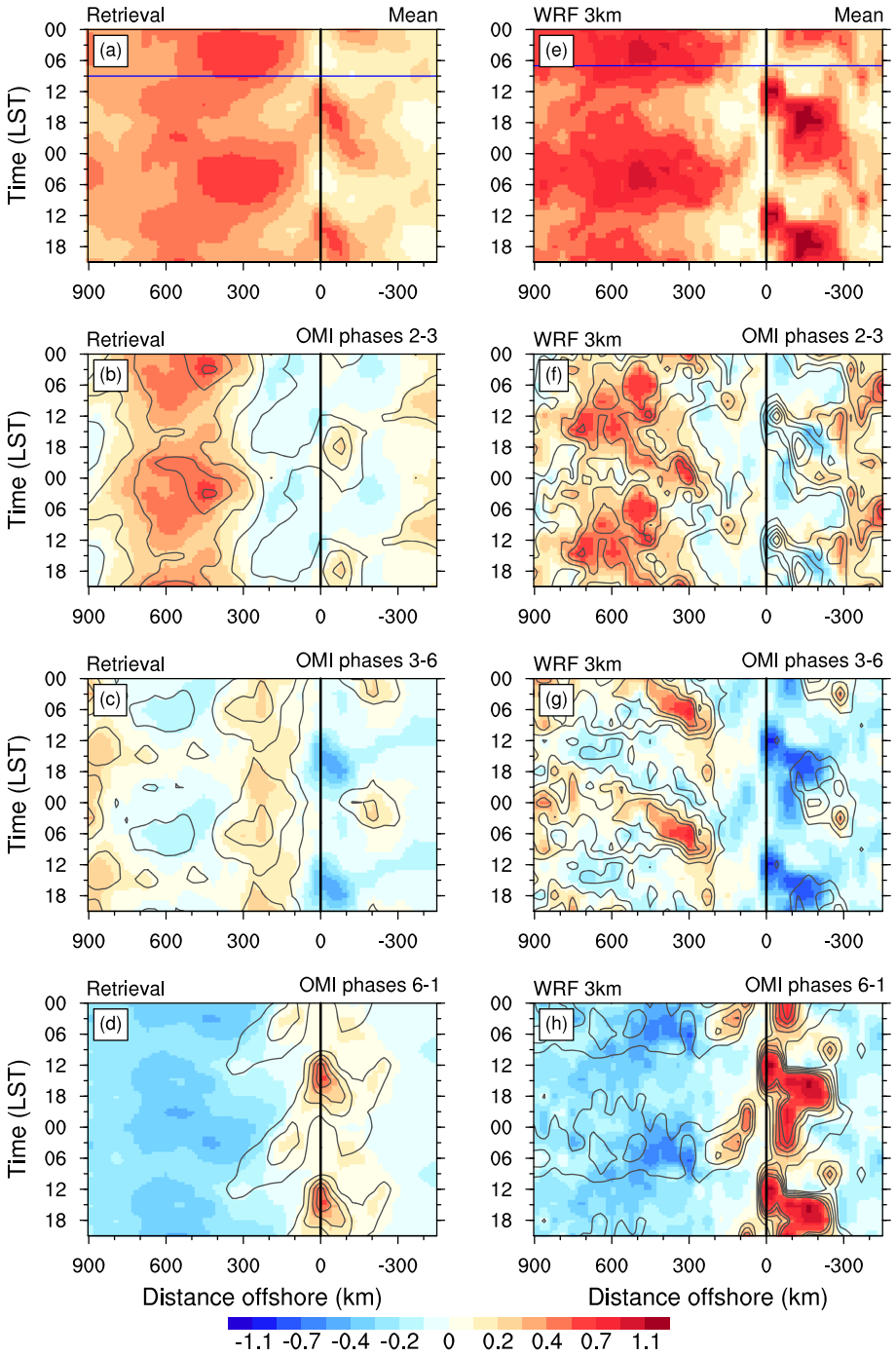

Figure 5. Diurnal cycle of precipitation (DCP, mm hr^{-1}) averaged along the transects over Sumatra. (a) Mean DCP during the entire simulation period. The blue horizontal line marks the initiation time of land precipitation. (b) Anomalous (colors) and total (contours, interval of 0.2 starting from 0.3) DCP during OMI Phases 2–3. (c, d) Same as (b) but for OMI Phase 3–6 and 6–1, respectively. (e–h) Same as (a)–(d) but from the simulations. Vertical solid lines indicate the location of peak terrain height and also the coastlines (zero distance). The horizontal axis is the distance from the coastline (km), and the positive distance denotes the southwestward direction. Time (vertical axis) has been repeated once to better show the diurnal cycle. Colors are unevenly distributed on the color bar.

4.2.1. Mean DCP

Over Sumatra, precipitation in the satellite retrievals is first initiated over mountain top at around 0900 LST and peaks at around 1800 LST then continuously migrates toward the northern plain with a phase speed of about 4.0 m s^{-1} (Figure 5a). The phase speed is calculated by tracking the propagation of the precipitation

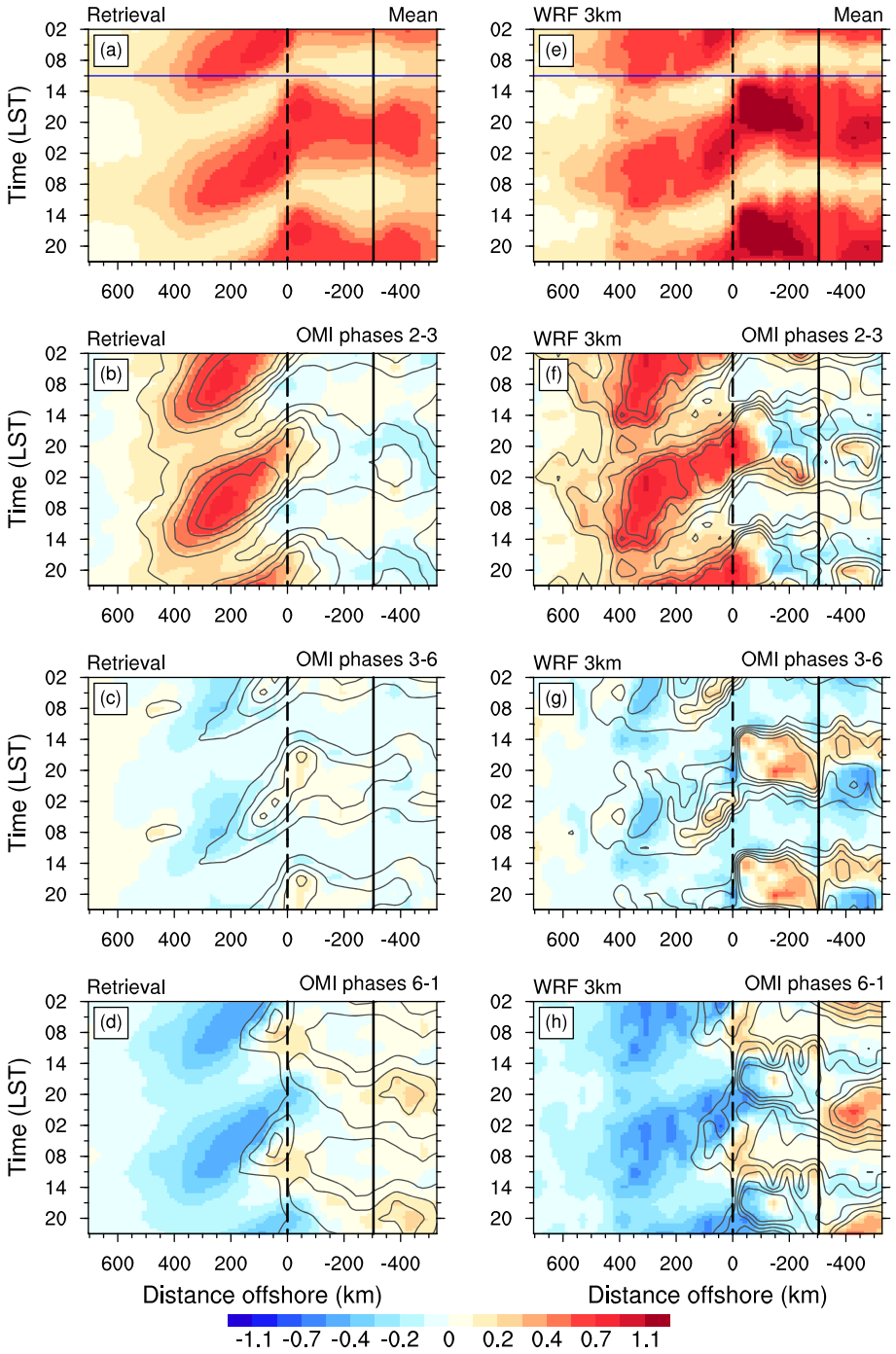

Figure 6. Same as Figure 5 but for Borneo. The vertical solid and dashed lines indicate the locations of the peak terrain height and the coastlines (zero distance), respectively. The positive distance (horizontal axis) denotes the northwestward direction.

maximum, similar to the method used by Yokoi et al. (2017, 2019). The precipitation southwest of Sumatra, however, tends to be persistent. For example, rainfall of 0.3 mm hr^{-1} can exist throughout the day. Using 10-year TRMM and CMORPH precipitation data, Vincent and Lane (2017) also found persistent rainfall southwest of Sumatra, especially during at preconditioning and active stages of the MJO over the MC. Oh et al. (2012) showed that the persistent rainfall may result from the wind-induced surface heat exchange mechanism proposed by Emanuel (1987) and Neelin et al. (1987). The persistent rainfall (as in Figure 5a) has a weak offshore propagation in the convective center (>0.4 mm hr^{-1}) occurring at around 0600 LST,

reflecting the diurnal variation of oceanic precipitation. These convective characteristics are generally reproduced by the simulations (Figure 5e). However, there are also some biases. For example, the simulations do not clearly reproduce the offshore propagation of the DCP. Both island and far-offshore rainfall are overestimated, while coastal rainfall is underestimated. In addition, in the simulations, convection is triggered immediately after sunrise around 0700 LST, which is 2 hr earlier than in the satellite retrievals.

In contrast to Sumatra, over Borneo with relatively low terrains and large island width (i.e., distance from mountain foothills to tops), island rainfall in the satellite retrievals (Figure 6a) is initiated over the mountain foothills and fast spreads toward the mountaintops. Offshore propagation (~8.1 m s^{-1}) northwest of Borneo can also be clearly observed. In the simulations (Figure 6e), the initiation and propagation of the DCP are well captured. As in the satellite retrievals, simulated rainfall tends to be initiated at around 1100 LST over the whole mountain, and its center (>0.8 mm hr^{-1}) displays similar inland spread. This indicates that the WRF model can well simulate the convective trigger over relatively lower topography. Vincent and Lane (2017) also suggested that the rainfall simulated by the WRF model may be too sensitive to high topography.

Over New Guinea, island rainfall from the satellite-derived data (Figure 7a) is first initiated near mountaintops as over Sumatra near 1100 LST and propagates and decays toward the two mountain foothills, where the rainfall peak near 20:00 to the south is stronger than that to the north. By tracking the propagation of rainfall maximum, we calculated that offshore rainfall propagates at two different speeds: ~5.5 m s^{-1} for the first 200 km and ~25.8 m s^{-1} after that, which is consistent with the results of Hassim et al. (2016) and Vincent and Lane (2016). The convective characteristics shown in satellite data are broadly reproduced by the simulations (Figure 7e), albeit with biases of ~3 hr too early in the convective trigger and overestimation of the amplitude and speed. The simulations also unrealistically produce a strong DCP 300 km away from the coast. This may be caused by (i) the convergence effect between the far offshore-propagating land breeze (Figure S1l) and the mean background easterly (see Figure 9) and (ii) the destabilization effect due to large offshore propagation of GWs.

4.2.2. DCP at the Three MJO Stages

We further examine the DCP at the various MJO stages (as depicted in section 3) to investigate the modulation of the local DCP by the MJO (e.g., large-scale variation in convection and circulation).

Precipitation undergoes clear variations during different MJO stages over both the land and nearby ocean of Sumatra, as seen from the satellite retrievals (Figures 5b–5d). For instance, persistent rainfall southwest of Sumatra appears only during OMI Phases 2–6 (i.e., local active conditions), which is in accordance with the MJO Phases 2–5 reported by Vincent and Lane (2017). The location also shifts from the far offshore regions during OMI Phases 2–3 (Figure 5b) to near the coast during OMI Phases 3–6 (Figure 5c), indicating the MJO modulation effect on the spatial distribution of the DCP anomalies. The island rainfall under these local active conditions, however, is very weak, especially near the mountaintops in the local convection decay condition (OMI Phases 3–6). During OMI Phases 6–1 (i.e., local suppressed conditions), less cloudy and less windy conditions prevail near Sumatra (Figures 3c), leading to very weak oceanic rainfall, while for the mountaintop region, the amplitude of the DCP is largely increased (Figure 5d). The offshore-propagating rainfall with a speed of about 4.1 m s^{-1} is clearly isolated under these local suppressed conditions. More interesting is that in OMI Phases 2–3, which feature local convection growth conditions (Figure 5b), island precipitation is triggered at around 1200 LST, which is 3 hr later than that under local suppressed conditions (Figure 5d). The above variations of the DCP over Sumatra (including the timing, amplitude, and propagation) under different MJO conditions are well simulated (Figures 5f–5h), albeit with overestimated amplitude over land and far offshore regions and underestimation near the coast in OMI Phases 3–6 (Figure 5g).

In the satellite retrievals (Figures 6b–6d), the most evident DCP variation around Borneo is over the northwest coast and oceanic regions, where very high precipitation and much amplified offshore propagation occur exclusively during OMI Phases 2–3 (i.e., local convection growth conditions) (Figure 6b). The weakest offshore propagation is during OMI Phases 6–1, which feature local suppressed conditions (Figure 6d). Over the interior regions of the island, although the DCP variation is not as large as that over the coastal and oceanic regions (Kanamori et al., 2013), the amplitude is generally larger under the local suppressed conditions, especially over the southeast plain of Borneo. With the passing of the MJO, there is also a tendency for the

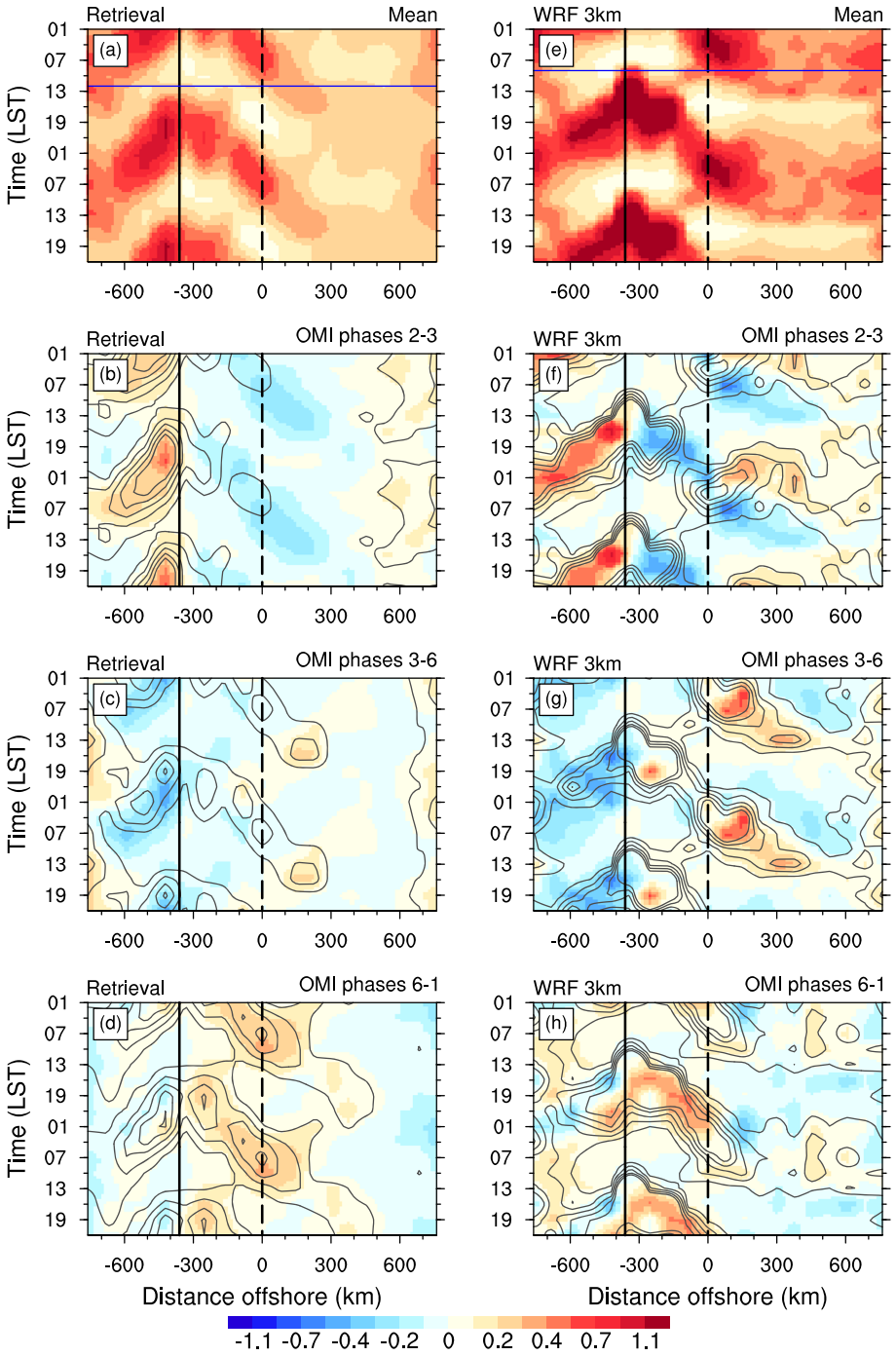

Figure 7. Same as Figure 6 but for New Guinea. The positive distance (horizontal axis) denotes the northeastward direction.

enhanced island rainfall to shift from the northwest plain toward the southeast plain. In contrast to Sumatra, which is characterized by very steep topography, the timing of the DCP over the relatively flat island of Borneo shows a weak sensitivity to the MJO. Using the cloud-resolving simulations, Riley Dellaripa et al. (2019) also pointed out that the variation of the timing of the island DCP over Luzon, Philippines, under local active versus suppressed TISO conditions in a flat-topographic run (similar to Borneo) was weaker than that in an elevated-topographic run (similar to Sumatra). The aforementioned characteristics of DCP variations are well reproduced by our simulations (Figures 6f–6h), although with slightly stronger intraseasonal variation in island rainfall.

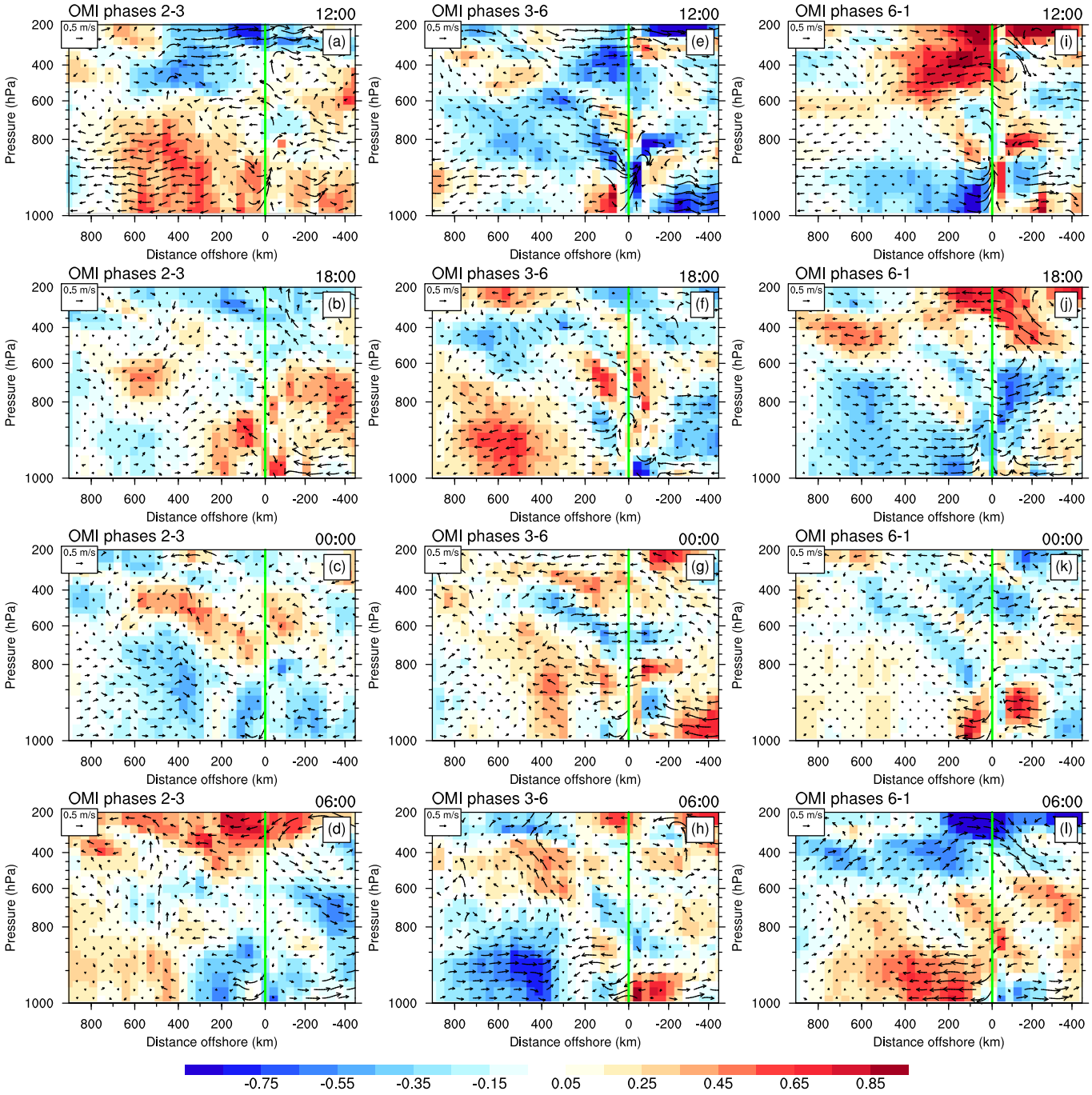

Figure 8. Height-distance cross sections averaged along the transects over Sumatra (Figure 1) for wind vector anomalies (m s^{-1}) in the horizontal speed (shading; m s^{-1}) at (from the top row down) 12:00, 18:00, 0:00, and 06:00 LST during OMI Phases (a–d) 2–3, (e–h) 3–6, and (i–l) 6–1 stages of the MJO. Vertical dashed lines indicate the location of the peak terrain height. Positive distance (horizontal axis) is southwestward.

For New Guinea, as seen from the satellite-based rainfall shown in Figures 7b–7d, the two offshore-propagating rainfall branches again have different representations at different MJO stages. Southward propagation is the most evident during OMI Phases 2–3 (i.e., local preconditioning conditions) (Figure 7b), while northward propagation dominates during OMI Phases 6–1 (i.e., local suppressed conditions) (Figure 7c), forming a unique dipolar structure in the DCP anomalies (Rauniyar & Walsh, 2013). This suggests that with variation in the large-scale background of the MJO, the enhanced DCP also shows a systematic shift from the west to the east coasts of the major islands. During OMI Phases 3–6 (i.e., local

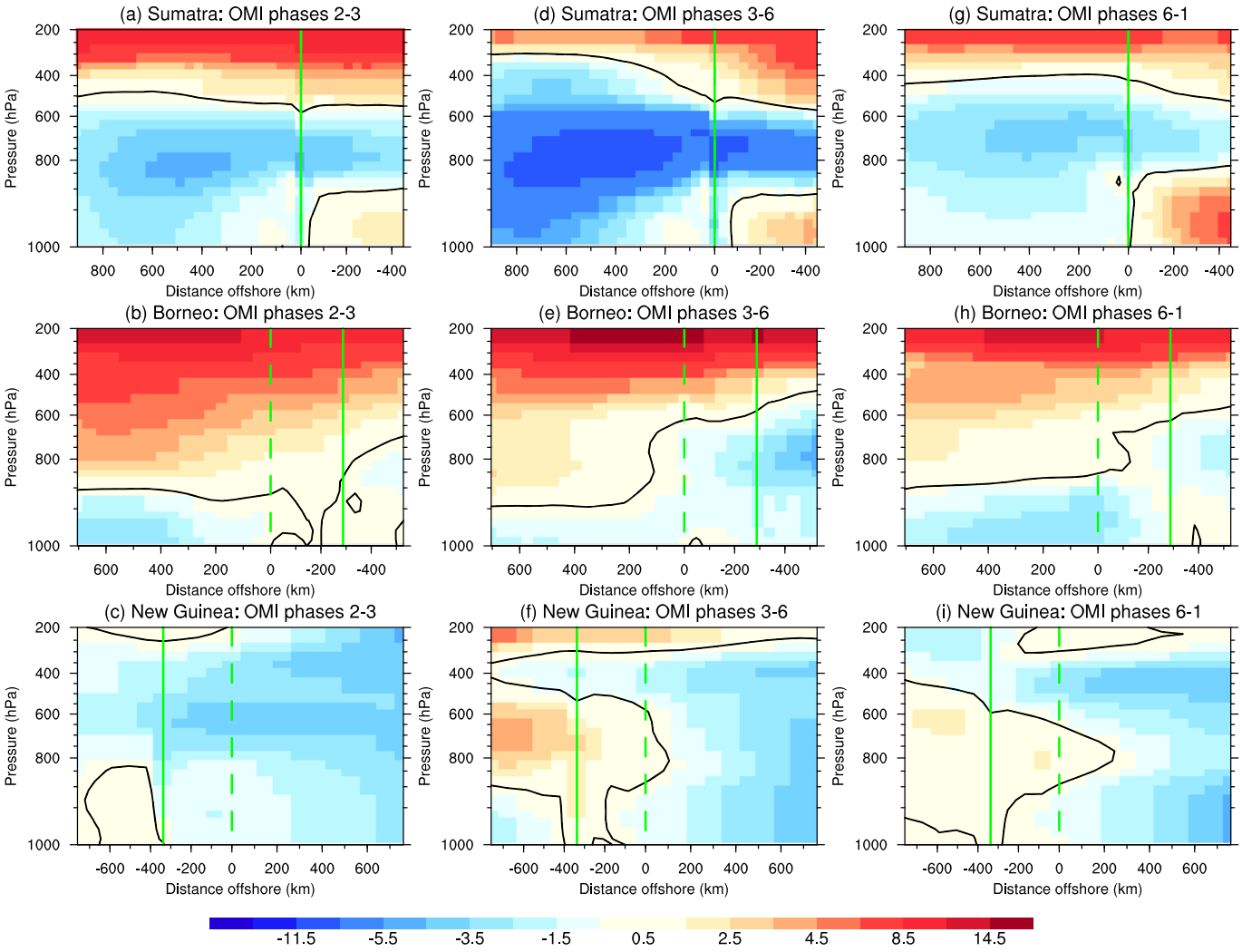

Figure 9. Height-distance cross sections averaged along the transects over (a, d, and g) Sumatra, (b, e, and h) Borneo, and (c, f, and i) New Guinea for the daily mean horizontal offshore (red) and onshore (blue) winds (zero shown by thick gray contours) during the OMI Phases (a–c) 2–3, (d–f) 3–6, and (g–i) 6–1. Vertical dashed lines indicate the location of the peak terrain height. Note the uneven values marked below the color bar. Positive distance (horizontal axis) is southwestward, northward, and northeast for Sumatra, Borneo, and New Guinea, respectively.

active conditions) (Figure 7c), however, both island and near-coast rainfall are largely reduced, while the rainfall far offshore shows a positive anomaly. Due to the high topography of New Guinea, the timing of the island DCP is again later under the local active condition (Figure 7c) than under the local preconditioning (Figures 7b) and suppressed conditions (Figure 7d). In the simulations (Figures 7f–7h), the intraseasonal variations of the DCP are also well captured but with a faster speed in offshore propagation, especially for the southward propagating branch. Similar to Figure 7e, the DCP anomalies beyond 300 km from the coast are also slightly overestimated.

5. Mechanisms of the MJO Modulation

In this section, we analyze both the large-scale conditions and the mesoscale circulations to investigate the underlying mechanisms by which the MJO contributes to the DCP variations depicted in section 4.2.2.

5.1. Valley Winds and Sea Breezes

5.1.1. Simulations

Figure 8 shows the diurnal variations of vertical circulations and their anomalies relative to the mean of the entire simulation period averaged along the transects over Sumatra at the three MJO stages. At 1200 LST

(Figures 8a, 8e, and 8i), land breezes are dominant over the far offshore and northern plain areas of Sumatra, while the onshore wind has been excited near the mountaintop region. Because the southwest coastline is very close to the mountain ridge, sea breezes cannot be separated unambiguously from the valley winds southwest of Sumatra. By contrast, over the northeast plain, there is clear divergence between onshore and offshore winds. The unique southwest-northeast contrast implies that the valley winds to the north should be more important than the sea breezes in contributing to the early triggering of island rainfall over Sumatra. This is also seen by Wu et al. (2009), who compared true and flat topographic simulations focusing on Sumatra (their Figures 4 and 9). Without high topography, the valley winds northeast of Sumatra disappear, and island precipitation becomes weak and nonorganized. Although these circulation patterns at 1200 LST are generally similar at different MJO stages, their intensities are distinct (refer to the anomalies shown by the color shading). For example, both the valley winds to the north and the onshore winds (valley wind plus sea breeze) to the south are the strongest during OMI Phases 6–1 (Figure 8i), and the weakest during OMI Phases 3–6 (Figure 8e). In the late afternoon at 1800 LST, the circulation patterns at all MJO stages have turned to sea breeze, especially during OMI Phases 6–1, which are characterized by much stronger and deeper onshore wind southwest of Sumatra (Figure 8j). The exception is the strengthened land breeze during OMI Phases 3–6 (Figure 8f). Therefore, the enhanced valley winds and sea breezes are crucial in explaining the strongest triggering and evolution of the island DCP under local suppressed conditions (i.e., OMI Phases 6–1) over Sumatra (Figure 5).

Why is the intensity of valley winds and sea breezes distinct at different MJO stages over Sumatra? This can be understood from two aspects. First, a less cloudy environment prevails during OMI Phases 6–1 (Figure 3d), and the radiative heating over land (especially over mountaintops) during the daytime can be further amplified, leading to an increased surface temperature gradient onshore and thus strengthened valley winds and sea breezes. The second explanation is the inverse relationship of the ambient wind and the amplitude of the diurnal cycle (e.g., Natoli & Maloney, 2019; Qian et al., 2010, 2013; Wang & Sobel, 2017). To facilitate discussion, we draw vertical profiles of daily mean winds along the transects over Sumatra averaged over different OMI phases (Figures 9a, 9d, and 9g). It can be clearly seen that due to the modulation of the MJO, the middle- to low-level westerly winds (blue shading) are the strongest during OMI Phases 3–6 (Figure 9d) and the weakest during OMI Phases 6–1 (Figure 9g). Accordingly, the most strengthened diurnal winds occur in OMI Phases 6–1 (i.e., local suppressed conditions). However, in OMI Phases 2–3 (i.e., local convection decay conditions), the diurnal winds should be largely weakened.

The diurnal variations of the vertical circulation patterns from early to late afternoon over Borneo (Figure 10) are generally similar to that over Sumatra. The intraseasonal variation in the amplitude of the diurnal winds, however, is not as strong as in Figure 8, which may partially explain the weak sensitivity of the island DCP over Borneo to the modulation of the MJO (Figure 6). This is also in agreement with S. Wang and Sobel (2017), who revealed the weakening of the extent of variation in the island DCP due to the change in large-scale wind with decreasing topography. A major difference between Borneo and Sumatra is the manner in which convection is triggered. As we can see from Figures 10a, 10e, and 10i, there are only penetrating sea breeze fronts (SBFs) with updraft aloft over the flat island of Borneo, instead of the first excitation of valley winds over the high topography of Sumatra (especially northeast of Sumatra). This implies that convective triggering may transfer from SBFs to valley winds because of the terrain elevation. Focusing on Sumatra, for example, Wu et al. (2009) also found that a regional high-resolution model could not reproduce mountain-valley wind when the topography was removed. Our results focusing on the much higher mountain of New Guinea (i.e., the control run plus the sensitivity experiment) will provide a chance to further validate this hypothesis.

Figure 11 shows the diurnal variation of the vertical circulation patterns over and surrounding New Guinea, an island with the maximum terrain height greater than 3,000 m (Figure 1). As expected, the upslope winds are again clearly observed near the mountaintop region with deep convection aloft at 1600 LST (Figures 11a, 11e, and 11i), which suggests the key role of valley winds in exciting the island DCP. Combined with the middle- to low-level mean winds shown in Figures 9c, 9f, and 9i, a striking feature in the anomalous diurnal circulation can be found: The valley winds and sea breezes tend to be enhanced over the lee side of the island, in agreement with Qian et al. (2013), although their study focused on the Borneo. For example, at 1600 LST, stronger than normal onshore winds over the south plain of New Guinea during OMI Phases

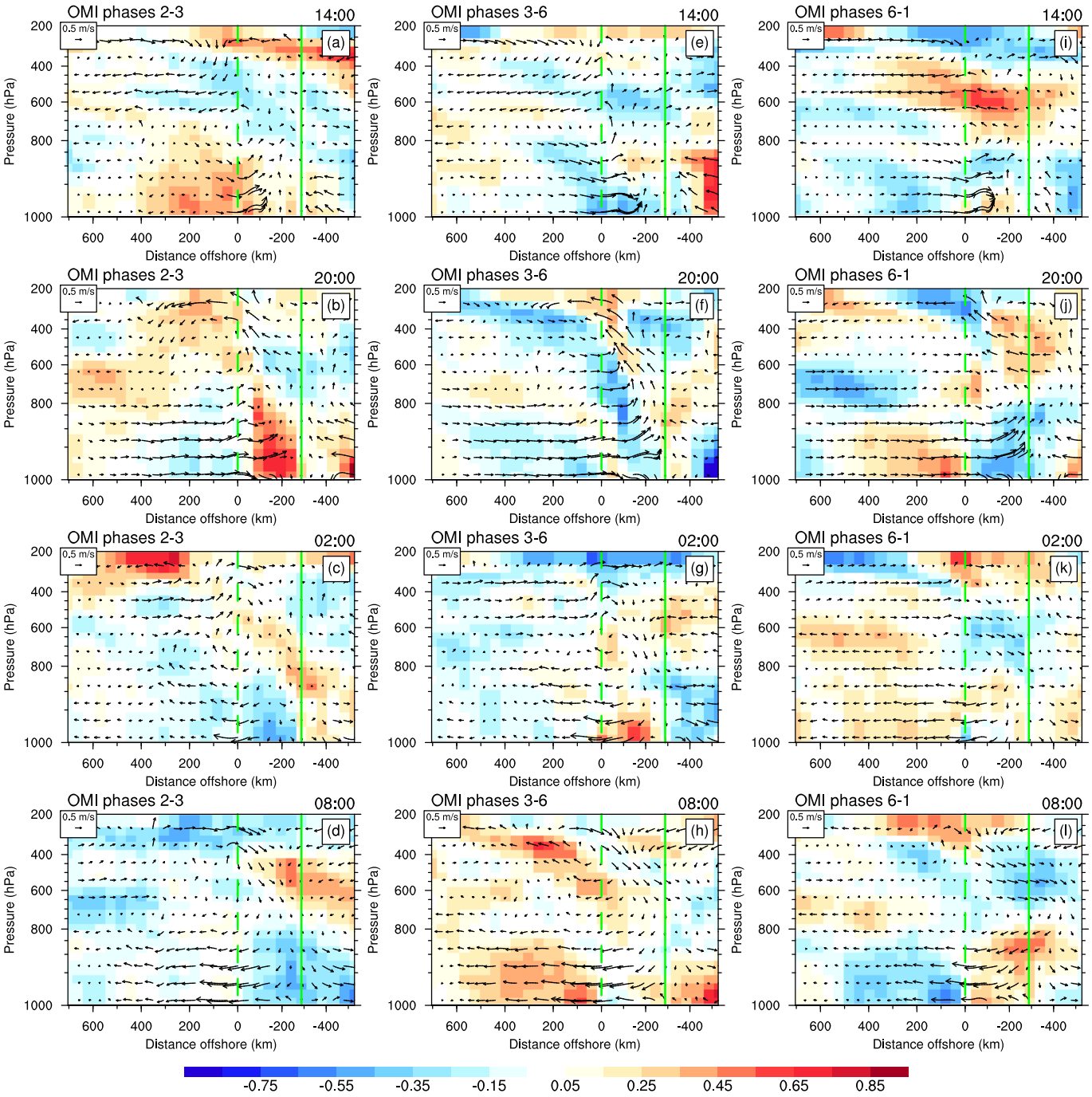

Figure 10. Same as Figure 8 but for Borneo at different LSTs. The vertical solid and dashed lines indicate the locations of the peak terrain height and the coastlines (zero distance), respectively. Positive distance (horizontal axis) is northwestward.

2–3 can be observed (Figure 11a), and this induces more moisture convergence and thus convection by interacting with the prevailing low-level easterly winds (Figure 9c). By contrast, during OMI Phases 6–1 (Figure 11i), the strengthened onshore winds prevailing north of New Guinea should support more convective initiation there by converging with low-level offshore winds (Figure 9i).

5.1.2. Sensitivity to Topography

The results presented above suggest the critical role of steep topography in influencing the DCP through the early excitation of valley winds. To further confirm this hypothesis, we compare the control simulations and

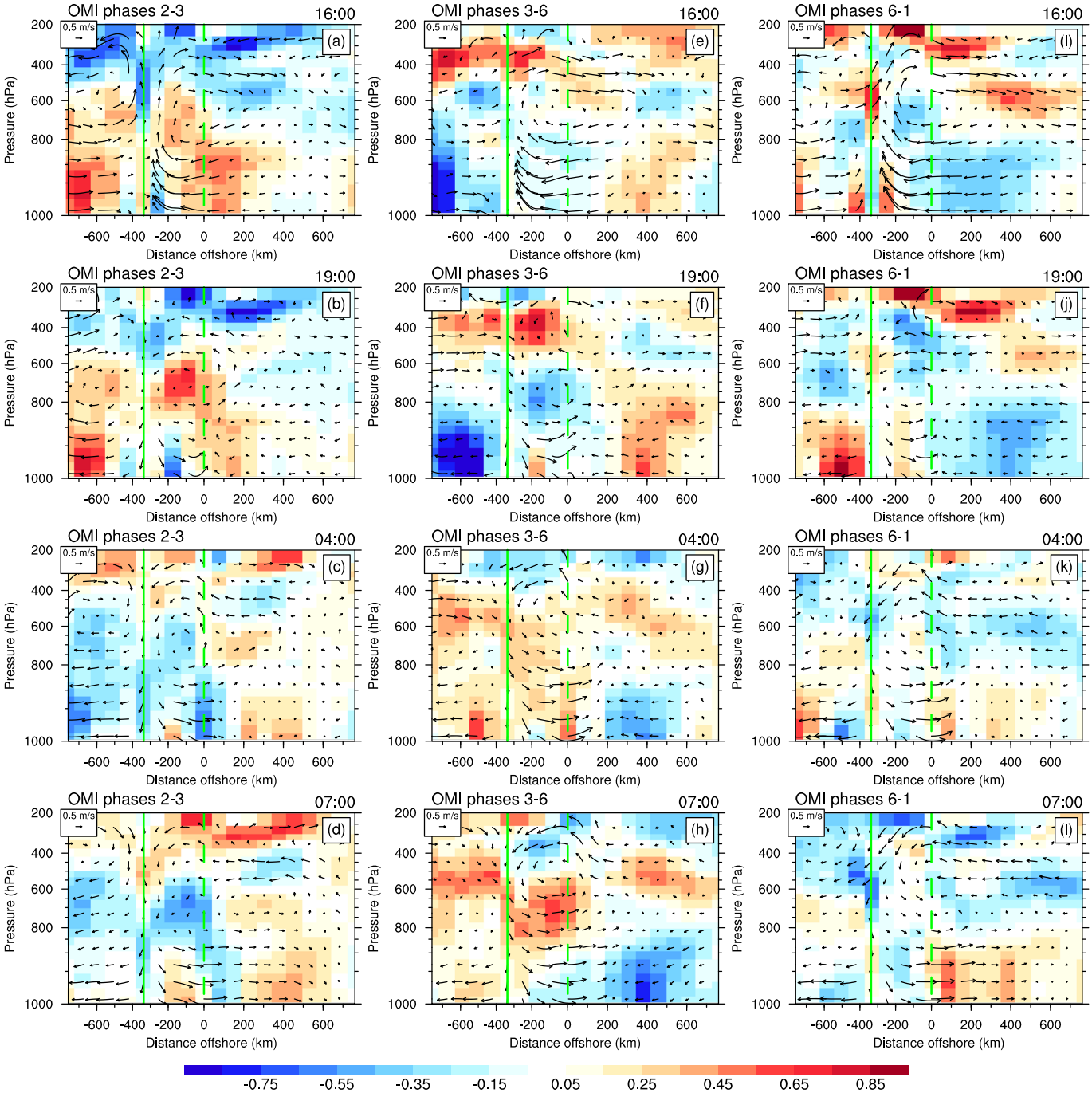

Figure 11. Same as Figure 8 but for New Guinea at different LSTs. Positive distance (horizontal axis) is northeastward.

REDUCE_TOPO_RUN. Composite maps of the DCP and anomalous diurnal 10-m winds during 16–20 January 2018 in the two sets of simulations are shown in Figures 12 and 13, respectively. In the control simulations, as seen clearly in Figure 12, rainfall is first initiated at 1000–1300 LST along the mountaintops in central New Guinea, consistent with Figure 7e. Accompanying the triggering of island precipitation, the diurnal 10-m wind anomalies also show early excitation of valley winds along the mountaintop region at 1000–1300 LST. In contrast, the coastal diurnal winds at this time, especially those northeast of New Guinea, are still dominated by land breezes. This suggests that the initial triggering of island convection over the mountaintop should be attributed to the convergence of valley winds. During 1300–1600 LST, the

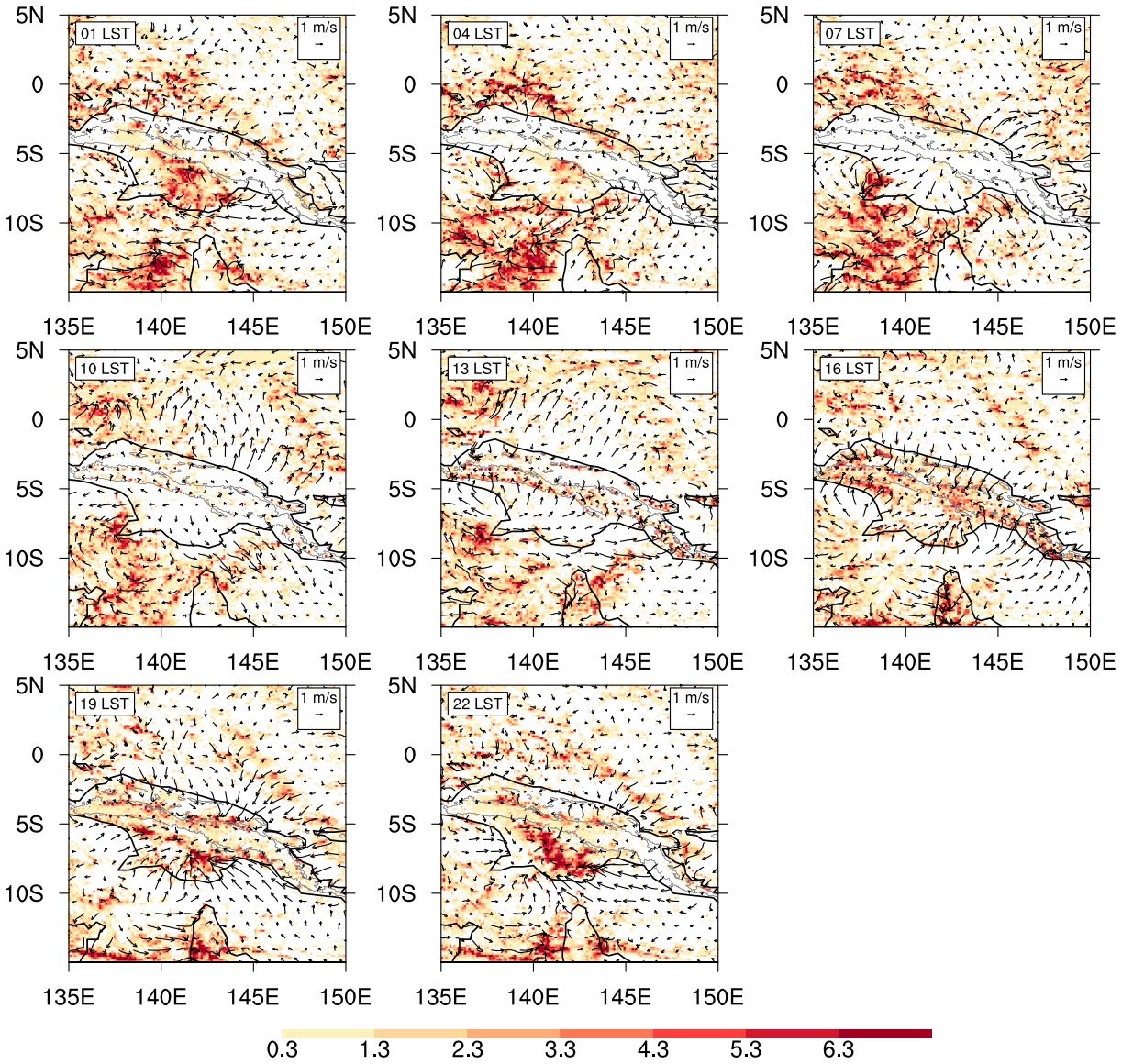

Figure 12. Composite diurnal cycle of simulated precipitation (shading) and 10-m wind (vector) during the period of 16–20 January 2018. To highlight the diurnal variation, the daily mean was removed from 10-m wind. Gray contours represent the terrain height of 0 (coastlines) and 600 m.

land rainfall grows and expands continuously due to further excitation of sea breezes and/or cumulus merger processes (Qian, 2008). After 1600 LST, as expected from Figure 7e, the island rainfall splits into two branches and migrates toward the north and south plains, respectively.

In REDUCE_TOPO_RUN (Figure 13), it is interesting to find that there is no organized rainfall initiation over the island until 1600 LST, which indicates that the existence of steep topography in reality should be responsible for the earlier triggering of island convection. In addition, the initiation region of land rainfall is mainly over the northern plain of New Guinea, instead of the mountaintop region in reality, very similar to the scenario over the flat island of Borneo. Moreover, a striking feature accompanies the triggering of land rainfall: Evident SBFs are seen along the northern coast. This suggests that without steep topography, island rainfall will be dramatically triggered over the mountain foothill region by the penetrating SBFs. In addition, the rain band initiated by the SBFs does not exhibit split propagation, as shown in Figure 12, but merely manifests as progressive migration toward the south plain due to the prevailing easterly wind (Figure 2). Note that without steep topography, the rainfall over the southeasternmost region of New Guinea is also initiated later (at 1300 LST) to the south plain due to the penetrating SBFs.

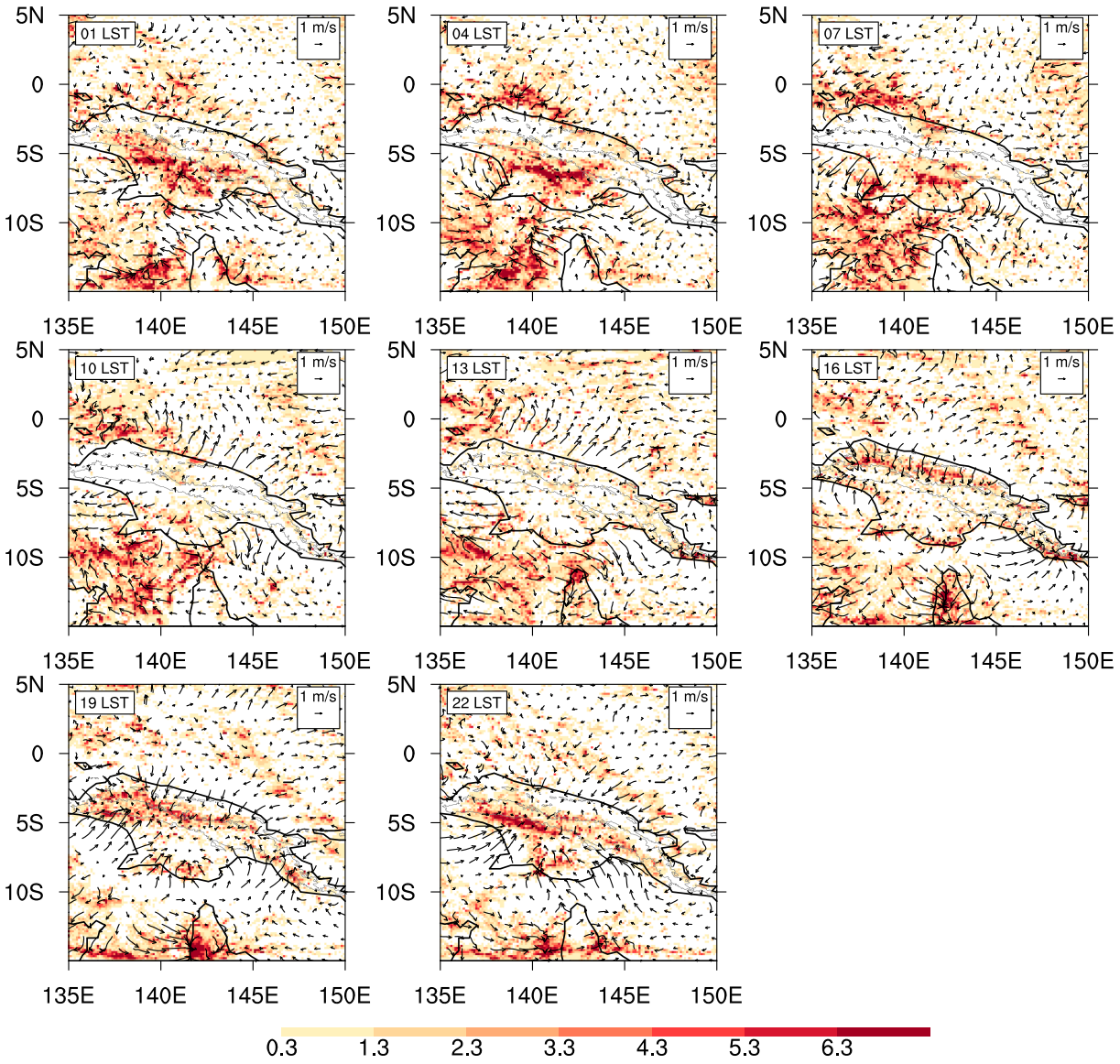

Figure 13. Same as Figure 12 but for the REDUCE_TOPO_RUN.

Overall, results from the sensitivity experiment show that the role of steep topography is to trigger island precipitation over the mountain top region earlier (by 3–6 hr) through the induced valley winds. Without steep topography, rainfall will be triggered later near the mountain foothills through the penetration of SBFs.

5.2. GWs

GWs provide another potential mechanism for offshore propagation of diurnal rainfall, especially related to nocturnal convective activities (e.g., Hassim et al., 2016; Love et al., 2011; Mapes et al., 2003; Vincent & Lane, 2016; Wu et al., 2009; Yokoi et al., 2017). Love et al. (2011) pointed out that statistically there are two kinds of GWs in the deep tropics that respond to different vertical diabatic heating profiles. The first kind is the deep internal GW responding to the deep convective heating of early afternoon over land. These deep GWs propagate offshore swiftly and cause deep warming and stabilization in the column through adiabatic descent in the leading edge of wave fronts, thereby suppressing oceanic convection during the daytime. The second kind is the slow high-order GW forced by a stratiform-type heating profile (with heating and cooling over and below the melting level, respectively), which is dominant during later afternoon and early evening. These GWs could destabilize the offshore atmosphere and support the oceanic nocturnal convection

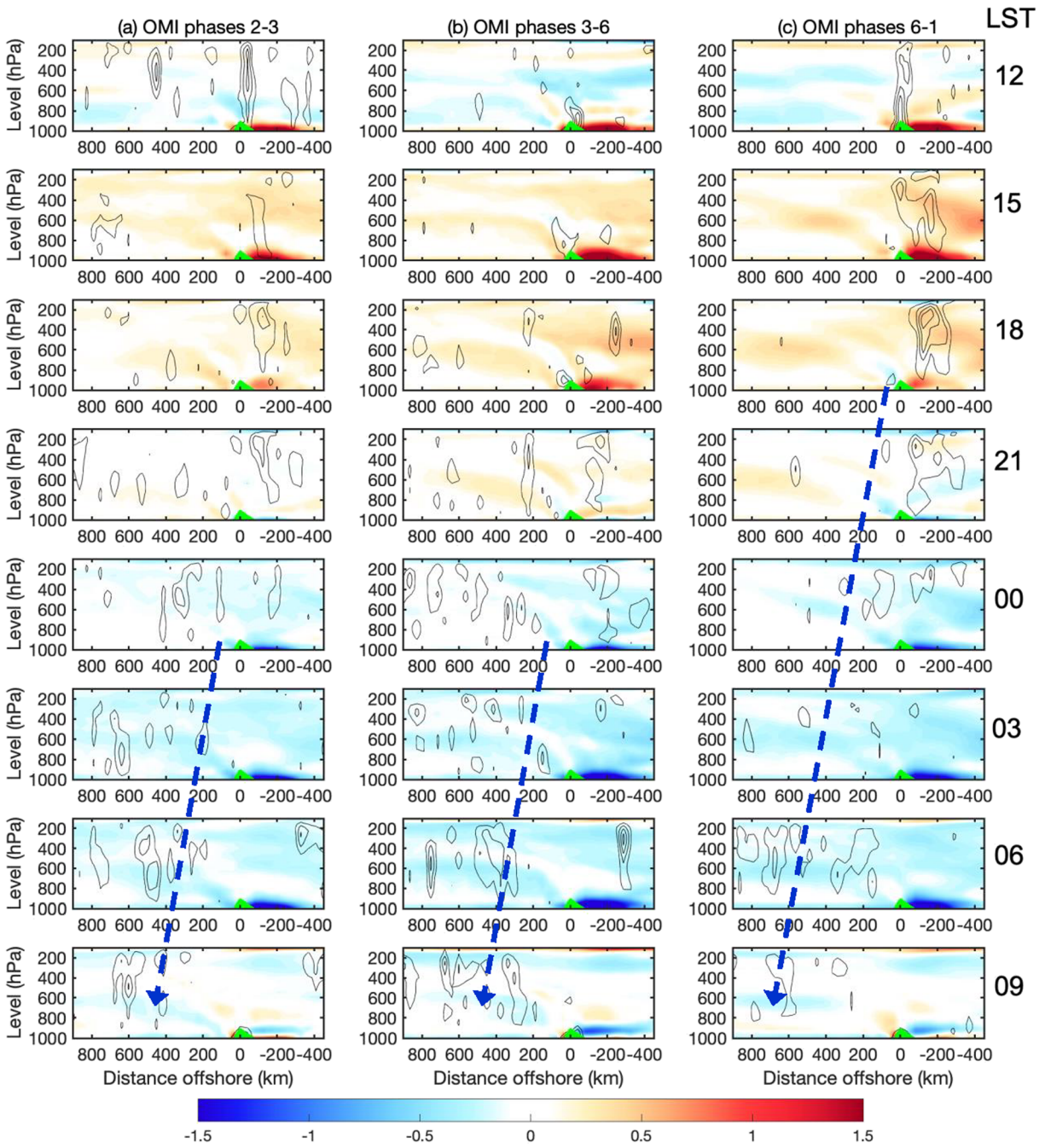

Figure 14. Height-distance cross sections of anomalous temperature (shading, K) and upward vertical pressure velocity (contour shown from 0.2 with interval of 0.5, ×20 m s^{-1}) averaged over the transects of Sumatra (Figure 1) during the OMI Phases (a) 2–3, (b) 3–6, and (c) 6–1 at different LSTs (marked at the right). The dashed arrows track roughly the offshore propagation of cold gravity wave signals (i.e., outward and upward spreading of negative temperature anomalies). The mean terrain height (hPa) averaged over the transects is also shown at the bottom of each panel. Positive distance (horizontal axis) is southwestward.

initiation through the upward and outward spreading of cold temperature anomalies and outflows (or land breezes) aloft seeding along the coastal areas. Here, we apply the GW mechanisms to explain the different offshore propagations of the DCP at different MJO stages. In Figures 14–16, the vertical velocity anomaly is used to represent convective activities, and the GW responses are represented by the anomalous temperature and land breezes shown in Figures 8, 10, and 11.

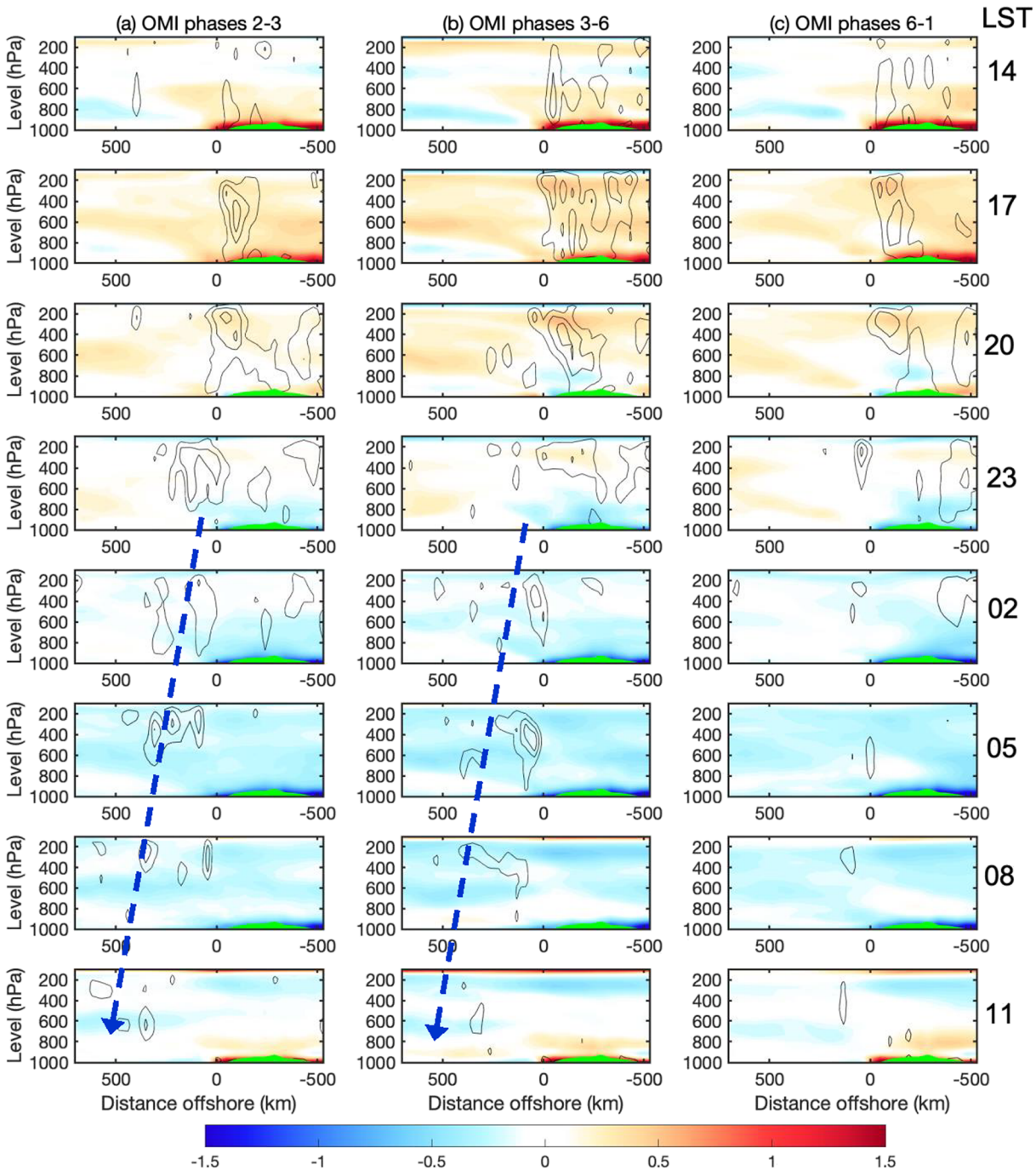

Figure 15. Same as Figure 14 but for Borneo. Positive distance (horizontal axis) is northwestward.

The excitation of island convection over Sumatra occurs at 0900 LST due primarily to the convergence associated with valley winds (Qian, 2008) as seen in Figure 14. The convection reaches its peak at noon and then gradually turns into a top-heavy structure with stratiform rainfall. The time evolution of the vertical structure in the convective activity is quite similar to that reported by Love et al. (2011). Because deep convection in early afternoon and stratiform rainfall in late afternoon are much stronger during OMI Phases 6–1 (Figure 14a), both the warm and cold signals of the GW undergo evident offshore propagation. For example, a cold temperature anomaly appears southwest of Sumatra at 1800 LST during OMI Phases 6–1, while the other two MJO stages (Figures 14b and 14c) are still dominated by positive temperature anomalies. This

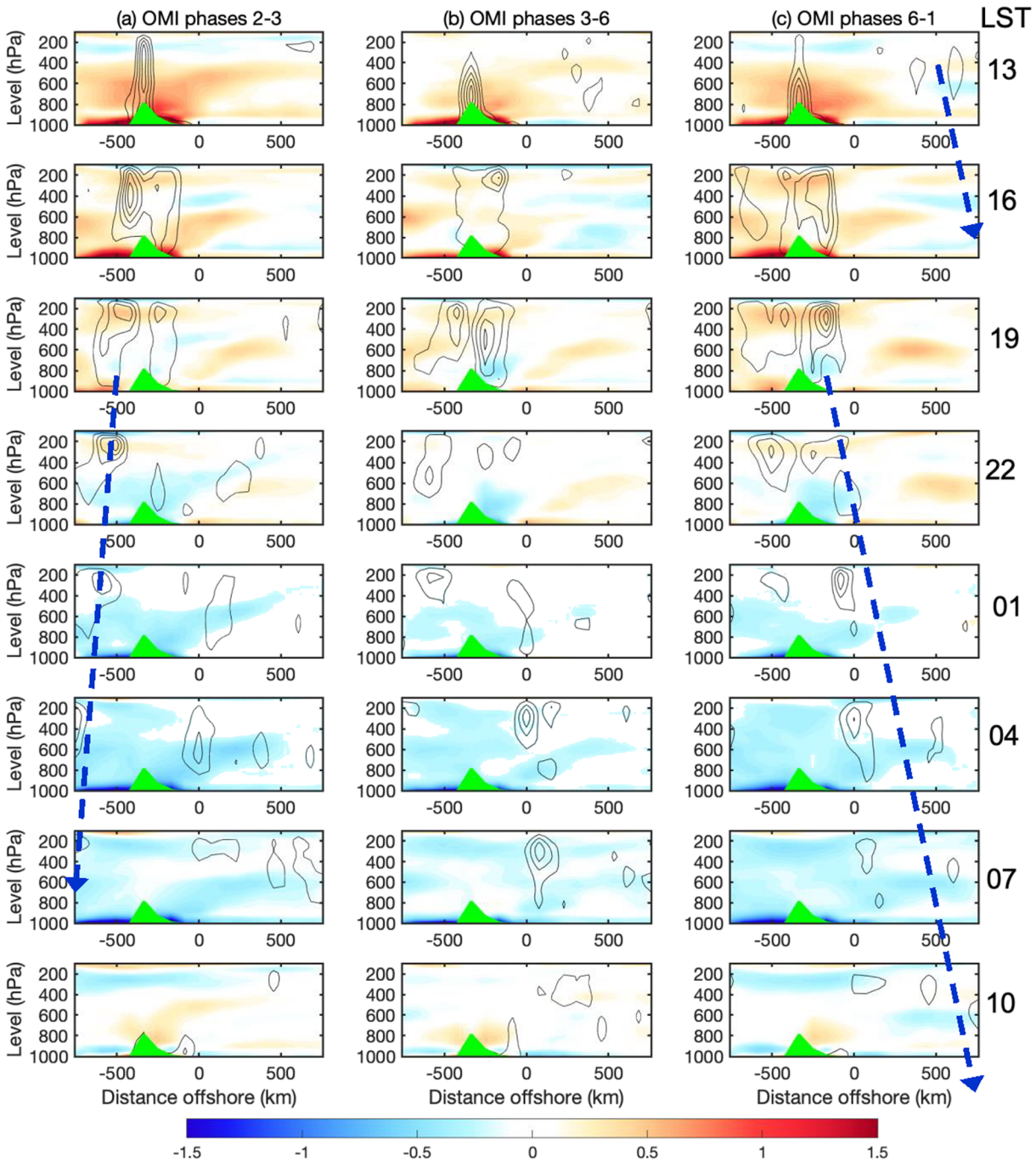

Figure 16. Same as Figure 14 but for New Guinea. Positive distance (horizontal axis) is northeastward.

cold temperature anomaly can develop and propagate far enough to destabilize the offshore atmosphere. This cold GW signal can also be clearly reflected in cold outflow, that is, the land breeze occurring after 1800 LST. As seen in Figures 8k and 8i, the land breeze off the southwest coast of Sumatra at 0000 LST is much stronger during OMI Phases 6–1 and keeps growing and migrating offshore at 0600 LST. The enhanced land breeze may induce stronger moisture convergence by interacting with the mean westerly wind in the lower troposphere (Figure 9g). Therefore, as depicted in Figure 5, coastal precipitation is triggered at around 1800 LST at the local suppressed stage but not the other stages.

For Borneo, the offshore DCP migration occurs only during OMI Phases 2–6, especially during OMI Phases 2–3, which feature local convection growth conditions (see Figure 6), as is well reflected by the diurnal variation of the ascent motion (see black contours in Figure 15). The exaggerated island rainfall over the northwest plain of Borneo during OMI Phases 3–6 (local convection decay conditions) is associated primarily with the overestimated updraft at 2000 LST (Figure 15b). The stratiform-type rainfall at 2300 LST during OMI Phases 2–3 is much stronger, leading to a well-developed cold signal of the GW propagating far offshore. During OMI Phases 6–1 under local suppressed conditions (Figure 15c), however, the cold signal of the GW has a weak outward and upward spread (blue shading in the offshore areas at 2300 and 0200 LST) due to the weak stratiform rainfall. The weakening of the cold GW signals can also be observed from the decreased cold outflow in OMI Phases 6–1 (Figure 10k). Therefore, the distinct behaviors of cold GW signals under different MJO conditions should partially contribute to different offshore propagations of the DCP northwest of Borneo, as shown in Figure 6.

Over New Guinea, convection at 1300 LST is the deepest during OMI Phases 2–3 (Figure 16a). At 1600 LST, deep convection begins to split into two branches propagating toward the northern and southern plains, respectively. It is interesting that the southern branch is stronger than the northern branch during OMI Phases 2–3, while the opposite is true in the other OMI phases (Figures 16b and 16c). These distinctive north-south asymmetries in different OMI phases correspond well with the interactions of enhanced land breezes and background winds of the MJO (Figures 9c, 9f, and 9i). The weak branch decays quickly, while the strong branch keeps migrating offshore, which is consistent with the distinctive offshore propagation of the DCP during different OMI phases (Figure 7). From 1600 to 1900 LST, deep convection converts into a stratiform-type mode, which is again stronger during OMI Phases 2–3 and 6–1 than OMI Phase 3–6. Therefore, the cold GW signals represented by the negative temperature anomalies and the outflowing land breezes (Figure 11) propagating to the north and south are stronger and more continuous from midnight to early morning before and after the local active conditions, suggesting that the convection-GW coupling mechanism is critical in explaining the offshore propagation of the DCP over New Guinea (Love et al., 2011; Vincent & Lane, 2016, 2018). During OMI Phases 2–3, a weak onshore-moving convection is triggered over the western Pacific at around 1900 LST and is further strengthened and maintained by the coupling with the offshore-propagating cold GW signals around 0100 LST.

5.3. Effect of Ambient Winds

Besides the aforementioned inverse relationship with the amplitude of the diurnal cycle, the ambient winds can also influence the DCP through the effects of advection (Ichikawa & Yasunari, 2006, 2008; Yanase et al., 2017), vertical wind shear (Yokoi et al., 2019), and terrain lifting (Chang et al., 2005).

Over the north slope of Sumatra (Figures 9a, 9d, and 9g), there are dramatic large-scale onshore winds in the boundary layer, and the vertical extent and magnitude increase from OMI Phases 2–3 to 6–1, which implies an increasing trend of the terrain lifting effect and thus more precipitation near mountain ridges under the local suppressed conditions of Sumatra (Figures 5d and 5h). Over the offshore area of Borneo, the ambient wind exhibits different vertical shear during different OMI phases (Figures 9b, 9e, and 9h). According to Yokoi et al. (2019), the calculated vertical wind shear between 950 and 800 hPa is about 3.0, 1.5, and 1.6 (m s^{-1}) (100 hPa)$^{-1}$ at the three stages, respectively. Note that LeMone et al. (1998) showed that a low-level wind shear stronger than 2.0 (m s^{-1}) (100 hPa)$^{-1}$ can trigger the regeneration of oceanic rainfall in the tropics. Therefore, a much-amplified offshore migration of the DCP is visible only under local convection growth conditions over Borneo (OMI Phase 2–3). The offshore mean wind in the midtroposphere at this MJO stage is also stronger than at the other MJO stages (6 m s^{-1} vs. 3 m s^{-1}), thereby advecting more rainfall offshore. Ichikawa and Yasunari (2008) found that the DCP propagation over New Guinea has a close association with the intraseasonal variation of low-level winds. As seen in Figures 9c, 9f, and 9i, the low-level winds are dominated by easterlies during OMI Phases 2–3 but by westerlies during the other OMI phases. Therefore, the DCP will propagate primarily westward under the local preconditioning condition, and the opposite is true under the local active and suppressed conditions of New Guinea (Figure 7).

6. Summary and Concluding Remarks

Understanding the DCP over the MC, especially its scale interactions with the MJO, is at the heart of the theme of atmospheric convection in the YMC project. Although this topic has been studied previously,

there are few explorations of how the interactions vary from island to island over the MC. In this study, high-resolution numerical simulations at a cloud-permitting scale (3 km) were conducted to explore the modulation of DCP by the large-scale convective and circulation conditions associated with a strong MJO event and the potential island dependence of the DCP characteristics. Sequential 30-hr simulations initiated at 0000 UTC every day were performed during the period of January–February 2018 when a strong MJO event passed over the MC. Comparisons with three satellite-based precipitation (TRMM, IMERG, and CMORPH) and three global reanalysis (NCEP FNL, ERA-I, and ERA5) products show that certain aspects of the diurnal wind and precipitation over the MC were reasonably simulated. Due to their coarse spatial resolution (~27 km), the global reanalysis data (especially ERA-I) show very weak diurnal variations in local circulation. In contrast, much useful information about the diurnal variability over the MC, for example, near the coastal regions and in the middle to upper troposphere, is available from the 3-km simulations. The internal consistency of the simulated circulation and convection provide a good opportunity to deeply explore the underlying mechanisms of the modulation of MJO on the DCP and also the variability between the three major islands of the MC (Sumatra, Borneo, and New Guinea). The main results are as follows:

1. The amplitude of the island DCP is enhanced during the local suppressed conditions of the MJO and reduced during local active conditions. The opposite is true over the ocean.
2. Modulated by the passing of the MJO, the enhanced island DCP also displayed a systematic shift from the west to the east coasts of the major islands, forming a unique dipolar structure in the anomalous DCP over land areas.
3. Convection was triggered differently across the three islands because of their distinctive topography. The DCP over the flat island of Borneo was first initiated over the mountain foothills through the penetration of SBFs. Over New Guinea, which is characterized by steep topography, the early excitation of valley winds was more responsible for the convective trigger. Due to the short distance between the southwest coastline and the mountain ridge in Sumatra, it was difficult to separate the role of SBFs and valley winds in exciting the island convection. However, the valley winds northeast of Sumatra were more unambiguously important than the SBFs and should partially contribute to the early excitation of island convection.
4. Results from the sensitivity experiments using reduced terrains confirmed that the existence of steep topography in New Guinea was responsible for the early (by 3–6 hr) triggering of island precipitation over the mountaintops through the early excitation of valley winds. However, without steep topography (above 600 m), the precipitation is triggered later near the mountain foothills through the penetration of SBFs.
5. The timing of the island DCP over Borneo showed a weak sensitivity to the variation of large-scale conditions of the MJO, in contrast to Sumatra and New Guinea, where the convective trigger under local active conditions was later (by ~3 hr) than under local suppressed conditions.
6. Both the large-scale conditions induced by the MJO and the mesoscale circulations were used to understand the intraseasonal variation of the DCP. Over Sumatra and New Guinea, the sea breeze was more sensitive to the MJO modulation than over Borneo; therefore, a more vigorous variation in the island DCP could be observed in both the satellite retrievals and simulations. Specifically, the island DCP over Sumatra was the strongest under the local suppressed conditions due to the much stronger sea/valley breezes and terrain lifting effect. The enhanced island DCP over the southern and northern New Guinea under the local preconditioning and suppressed condition could be explained by the strengthened sea/valley breezes over the lee side of the topography, the wind advection effect, and the destabilization effect induced by the offshore-propagating cold GWs.
7. The mechanisms for the intraseasonal variations of oceanic DCP also manifested as island-dependent characteristics. For example, the offshore migration of the DCP southwest of Sumatra was visible during the local suppressed period of MJO, which resulted mainly from the enhanced cold outflows associated with the stratiform rainfall-induced GW effects. The much amplified offshore migration of coastal and oceanic DCP under the local convection growth conditions northwest of Borneo was attributed primarily to the much larger low-level vertical wind shear and the wind advection effects. Over New Guinea, the wind advection effect and the cold GWs excited by the cooling of strong stratiform rainfall were responsible for the enhanced offshore migration of nocturnal precipitation under the local suppressed conditions.

Collectively, these results suggest that there is likely significant and potentially important island-to-island variability in the scale interaction between the DCP and MJO over the MC, which is driven essentially by variation in topography, island size, and orientation relative to the background wind patterns associated with a propagating MJO event. Our results also suggest that weather/climate models need to capture these finer-scale geographical details in order to completely resolve how the MJO interacts with the DCP over the MC and ultimately improve the prediction skill of MJO events when propagating across the MC.

In this study, however, we did not examine the possible upscale feedbacks of the DCP on the MJO. Previous studies have suggested that the DCP is important in explaining the barrier effect of the MC on MJO eastward propagation (e.g., Hagos et al., 2016; Ling et al., 2019; Majda & Yang, 2016; Oh et al., 2013; Zhang & Ling, 2017). The unique match between the leading edge of the large-scale MJO envelope and the eastward dispersion of the 2-day waves found in both the satellite observations and numerical simulations implies that the 2-day waves may serve as a potential drag on the MJO eastward propagation: Stronger destabilization should selectively occur to the east of the old convection. Moreover, the 2-day waves may breed from the upscale growth and organization of the westward propagating DCP (e.g., Chen & Houze, 1997; Ruppert et al., 2020; Ruppert & Zhang, 2019). Therefore, there may be a possible upscale feedback of the DCP on the MJO eastward propagation, where the role of the eastward regeneration of 2-day waves can be vital. Cloud-permitting models are useful tools to shed light on this interesting scientific question, which we are currently investigating. We hope to report the results in the future.

There are also caveats in this work. First, the cloud-permitting scale numerical simulations largely overestimated the magnitude of the DCP and showed somewhat earlier timing of the island DCP. These model biases, also seen in previous studies (e.g., Hassim et al., 2016; Love et al., 2011; Vincent & Lane, 2016, 2017), are especially obvious over and near steep topography. On the other hand, when satellite retrieval products are used to validate model simulations, their notable biases (e.g., Birch et al., 2015; Kikuchi & Wang, 2008; Lu et al., 2019) also need to be considered. Second, the documented regional variations of the island DCP under the modulation of the MJO and its close association with topographic features should be confirmed further by more sensitivity experiments. Along this line, most previous studies performed comparisons only between true topographic runs and runs with removed or elevated topography (e.g., Qian, 2008; Riley Dellaripa et al., 2019; Wu et al., 2009). Due to the intricacy of geographic settings and island geometry over the MC, it would be also interesting to consider the DCP variation in simulations with different island sizes, orientations, and coastline shapes. Finally, the numerical simulations in this study focused only on January–February 2018, and thus, the seasonal variations of the DCP cannot be investigated. To fully understand the multiscale interaction of the DCP with low-frequency variabilities, we also performed new simulations focusing on July 2017, during which an El Niño condition and a weak MJO event cooccurred. We expect totally different DCP characteristics over the MC as compared with this study, which will be reported in the future.

Data Availability Statement

The model experiments and postprocessing were conducted using the supercomputing clusters at the CHPC at the University of Utah. Daily interpolated OLRs were obtained from NOAA/OAR/ESRL PSD, Boulder, Colorado, USA (https://www.ersl.noaa.gov/psd/). The ERA-I analysis was from ECMWF (https://apps.ecmwf.int/datasets/data/interim-full-daily/levtype=sfc/). The NCEP FNL analysis was from the Research Data Archive at the National Center for Atmospheric Research, Computational and Information Systems Laboratory (https://doi.org/10.5065/D65Q4T4Z). OMI was downloaded from the website (https://www.esrl.noaa.gov/psd/mjo/mjoindex/). This is PMEL Contribution 5061.

Acknowledgments
The authors thank two anonymous reviewers for their constructive comments that helped improve this article. This study was supported by NOAA Award NA17OAR4310262.

References

Adames, Á. F., & Wallace, J. M. (2014). Three-dimensional structure and evolution of the MJO and its relation to the mean flow. *Journal of the Atmospheric Sciences*, *71*(6), 2007–2026. https://doi.org/10.1175/JAS-D-13-0254.1

Baranowski, D. B., Waliser, D. E., Jiang, X., Ridout, J. A., & Flatau, M. K. (2019). Contemporary GCM fidelity in representing the diurnal cycle of precipitation over the Maritime Continent. *Journal of Geophysical Research: Atmospheres*, *124*, 747–769. https://doi.org/10.1029/2018JD029474

Biasutti, M., Yuter, S. E., Burleyson, C. D., & Sobel, A. H. (2012). Very high-resolution rainfall patterns measured by TRMM precipitation radar: Seasonal and diurnal cycles. *Climate Dynamics*, *39*(1–2), 239–258. https://doi.org/10.1007/s00382-011-1146-6

Birch, C. E., Roberts, M. J., Garcia-Carreras, L., Ackerley, D., Reeder, M. J., Lock, A. P., & Schiemann, R. (2015). Sea-breeze dynamics and convection initiation: The influence of convective parameterization in weather and climate model biases. *Journal of Climate*, *28*(20), 8093–8108. https://doi.org/10.1175/JCLI-D-14-00850.1

Birch, C. E., Webster, S., Peatman, S. C., Parker, D. J., Matthews, A. J., Li, Y., & Hassim, M. E. E. (2016). Scale interactions between the MJO and the western Maritime Continent. *Journal of Climate*, *29*(7), 2471–2492. https://doi.org/10.1175/JCLI-D-15-0557.1

Chang, C. P., Harr, P. A., & Chen, H. J. (2005). Synoptic disturbances over the equatorial South China Sea and western Maritime Continent during boreal winter. *Monthly Weather Review*, *133*(3), 489–503. https://doi.org/10.1175/MWR-2868.1

Chang, C. P., Harr, P. A., McBride, J. O. H. N., & Hsu, H. H. (2004). Maritime continent monsoon: Annual cycle and boreal winter variability. *East Asian Monsoon*, 107–150. https://doi.org/10.1142/9789812701411_0003

Chen, S. S., & Houze, R. A. (1997). Diurnal variation and life-cycle of deep convective systems over the tropical Pacific warm pool. *Quarterly Journal of the Royal Meteorological Society*, *123*(538), 357–388. https://doi.org/10.1002/qj.49712353806

Dee, D. P., Uppala, S. M., Simmons, A. J., Berrisford, P., Poli, P., Kobayashi, S., et al. (2011). The ERA-Interim reanalysis: Configuration and performance of the data assimilation system. *Quarterly Journal of the Royal Meteorological Society*, *137*(656), 553–597. https://doi.org/10.1002/qj.828

Emanuel, K. A. (1987). An air-sea interaction model of intraseasonal oscillations in the tropics. *Journal of the Atmospheric Sciences*, *44*(16), 2324–2340. https://doi.org/10.1175/1520-0469(1987)044<2324:AASIMO>2.0.CO;2

Fujita, M., Kimura, F., & Yoshizaki, M. (2010). Morning precipitation peak over the Strait of Malacca under a calm condition. *Monthly Weather Review*, *138*(4), 1474–1486. https://doi.org/10.1175/2009MWR3068.1

Fujita, M., Yoneyama, K., Mori, S., Nasuno, T., & Satoh, M. (2011). Diurnal convection peaks over the eastern Indian Ocean off Sumatra during different MJO phases. *Journal of the Meteorological Society of Japan. Ser. II*, *89*, 317–330. https://doi.org/10.2151/jmsj.2011-A22

Gentemann, C. L., Donlon, C. J., Stuart-Menteth, A., & Wentz, F. J. (2003). Diurnal signals in satellite sea surface temperature measurements. *Geophysical Research Letters*, *30*(3), 1140. https://doi.org/10.1029/2002GL016291

Hagos, S. M., Zhang, C., Feng, Z., Burleyson, C. D., De Mott, C., Kerns, B., et al. (2016). The impact of the diurnal cycle on the propagation of Madden-Julian Oscillation convection across the Maritime Continent. *Journal of Advances in Modeling Earth Systems*, *8*(4), 1552–1564. https://doi.org/10.1002/2016MS000725

Hassim, M. E. E., Lane, T. P., & Grabowski, W. W. (2016). The diurnal cycle of rainfall over New Guinea in convection-permitting WRF simulations. *Atmospheric Chemistry and Physics*, *16*(1), 161–175. https://doi.org/10.5194/acp-16-161-2016

Hendon, H. H., & Woodberry, K. (1993). The diurnal cycle of tropical convection. *Journal of Geophysical Research*, *98*(D9), 16,623–16,637. https://doi.org/10.1029/93JD00525

Houze, R. A. Jr., Geotis, S. G., Marks, F. D. Jr., & West, A. K. (1981). Winter monsoon convection in the vicinity of north Borneo. Part I: Structure and time variation of the clouds and precipitation. *Monthly Weather Review*, *109*(8), 1595–1614. https://doi.org/10.1175/1520-0493(1981)109<1595:WMCITV>2.0.CO;2

Huffman, G. J., Bolvin, D. T., & Nelkin, E. J. (2015). Integrated Multi-satellitE Retrievals for GPM (IMERG) technical documentation. *NASA/GSFC Code*, *612*(47), 2019. https://pmm.nasa.gov/sites/default/files/document_files/IMERG_doc_190313.pdf

Huffman, G. J., Bolvin, D. T., Nelkin, E. J., Wolff, D. B., Adler, R. F., Gu, G., et al. (2007). The TRMM multisatellite precipitation analysis (TMPA): Quasi-global, multiyear, combined-sensor precipitation estimates at fine scales. *Journal of Hydrometeorology*, *8*(1), 38–55. https://doi.org/10.1175/JHM560.1

Hung, C. S., & Sui, C. H. (2018). A diagnostic study of the evolution of the MJO from Indian Ocean to Maritime Continent: Wave dynamics versus advective moistening processes. *Journal of Climate*, *31*(10), 4095–4115. https://doi.org/10.1175/JCLI-D-17-0139.1

Ichikawa, H., & Yasunari, T. (2006). Time–space characteristics of diurnal rainfall over Borneo and surrounding oceans as observed by TRMM-PR. *Journal of Climate*, *19*(7), 1238–1260. https://doi.org/10.1175/JCLI3714.1

Ichikawa, H., & Yasunari, T. (2008). Intraseasonal variability in diurnal rainfall over New Guinea and the surrounding oceans during austral summer. *Journal of Climate*, *21*(12), 2852–2868. https://doi.org/10.1175/2007JCLI1784.1

Jiang, Q. (2012). On offshore propagating diurnal waves. *Journal of the Atmospheric Sciences*, *69*(5), 1562–1581. https://doi.org/10.1175/JAS-D-11-0220.1

Jin, F., & Hoskins, B. J. (1995). The direct response to tropical heating in a baroclinic atmosphere. *Journal of the Atmospheric Sciences*, *52*(3), 307–319. https://doi.org/10.1175/1520-0469(1995)052<0307:TDRTTH>2.0.CO;2

Joyce, R. J., Janowiak, J. E., Arkin, P. A., & Xie, P. (2004). CMORPH: A method that produces global precipitation estimates from passive microwave and infrared data at high spatial and temporal resolution. *Journal of Hydrometeorology*, *5*(3), 487–503. https://doi.org/10.1175/1525-7541(2004)005<0487:CAMTPG>2.0.CO;2

Kanamori, H., Yasunari, T., & Kuraji, K. (2013). Modulation of the diurnal cycle of rainfall associated with the MJO observed by a dense hourly rain gauge network at Sarawak, Borneo. *Journal of Climate*, *26*(13), 4858–4875. https://doi.org/10.1175/JCLI-D-12-00158.1

Kikuchi, K., & Wang, B. (2008). Diurnal precipitation regimes in the global tropics. *Journal of Climate*, *21*(11), 2680–2696. https://doi.org/10.1175/2007JCLI2051.1

Kikuchi, K., & Wang, B. (2010). Spatiotemporal wavelet transform and the multiscale behavior of the Madden–Julian oscillation. *Journal of Climate*, *23*(14), 3814–3834. https://doi.org/10.1175/2010JCLI2693.1

Kiladis, G. N., Dias, J., Straub, K. H., Wheeler, M. C., Tulich, S. N., Kikuchi, K., et al. (2014). A comparison of OLR and circulation-based indices for tracking the MJO. *Monthly Weather Review*, *142*(5), 1697–1715.

Kiladis, G. N., Wheeler, M. C., Haertel, P. T., Straub, K. H., & Roundy, P. E. (2009). Convectively coupled equatorial waves. *Reviews of Geophysics*, *47*(2). https://doi.org/10.1029/2008RG000266

Lau, W. K. M., & Waliser, D. E. (2012). Intraseasonal variability in the atmosphere-ocean climate system. *Springer Science & Business Media*. https://doi.org/10.1007/978-3-642-13914-7

LeMone, M. A., Zipser, E. J., & Trier, S. B. (1998). The role of environmental shear and thermodynamic conditions in determining the structure and evolution of mesoscale convective systems during TOGA COARE. *Journal of the Atmospheric Sciences*, *55*(23), 3493–3518. https://doi.org/10.1175/1520-0469(1998)055<3493:TROESA>2.0.CO;2

Li, Y., & Carbone, R. E. (2015). Offshore propagation of coastal precipitation. *Journal of the Atmospheric Sciences*, *72*(12), 4553–4568. https://doi.org/10.1175/JAS-D-15-0104.1

Liebmann, B., & Smith, C. A. (1996). Description of a complete (interpolated) outgoing longwave radiation dataset. *Bulletin of the American Meteorological Society*, *77*(6), 1275–1277. https://www.jstor.org/stable/26233278

Ling, J., Zhang, C., Joyce, R., Xie, P. P., & Chen, G. (2019). Possible role of the diurnal cycle in land convection in the barrier effect on the MJO by the Maritime Continent. *Geophysical Research Letters*, *46*, 3001–3011. https://doi.org/10.1029/2019GL081962

Love, B. S., Matthews, A. J., & Lister, G. M. (2011). The diurnal cycle of precipitation over the Maritime Continent in a high-resolution atmospheric model. *Quarterly Journal of the Royal Meteorological Society*, *137*(657), 934–947. https://doi.org/10.1002/qj.809

Lu, J., Li, T., & Wang, L. (2019). Precipitation diurnal cycle over the Maritime Continent modulated by the MJO. *Climate Dynamics*, *53*(9–10), 6489–6501. https://doi.org/10.1007/s00382-019-04941-8

Madden, R. A., & Julian, P. R. (1971). Detection of a 40–50 day oscillation in the zonal wind in the tropical Pacific. *Journal of the Atmospheric Sciences*, *28*, 702–708. https://doi.org/10.1175/1520-0469(1971)028<0702:DOADOI>2.0.CO;2

Madden, R. A., & Julian, P. R. (1972). Description of global-scale circulation cells in the tropics with a 40–50 day period. *Journal of the Atmospheric Sciences*, *29*(6), 1109–1123. https://doi.org/10.1175/1520-0469(1972)029<1109:DOGSCC>2.0.CO;2.

Majda, A. J., & Yang, Q. (2016). A multiscale model for the intraseasonal impact of the diurnal cycle over the Maritime Continent on the Madden–Julian Oscillation. *Journal of the Atmospheric Sciences*, *73*(2), 579–604. https://doi.org/10.1175/JAS-D-15-0158.1

Mapes, B. E., Warner, T. T., & Xu, M. (2003). Diurnal patterns of rainfall in northwestern South America. Part III: Diurnal gravity waves and nocturnal convection offshore. *Monthly Weather Review*, *131*(5), 830–844. https://doi.org/10.1175/1520-0493(2003)131<0830:DPORIN>2.0.CO;2

Margono, B. A., Potapov, P. V., Turubanova, S., Stolle, F., & Hansen, M. C. (2014). Primary forest cover loss in Indonesia over 2000–2012. *Nature Climate Change*, *4*(8), 730. https://doi.org/10.1038/nclimate2277

Matthews, A. J. (2008). Primary and successive events in the Madden–Julian Oscillation. *Quarterly Journal of the Royal Meteorological Society*, *134*(631), 439–453. https://doi.org/10.1002/qj.224

McBride, J. (1998). Indonesia, Papua New Guinea, and tropical Australia: The Southern Hemisphere monsoon. *Meteorology of the Southern Hemisphere*, 89–99. https://doi.org/10.1007/978-1-935704-10-2_3

Miller, S. T. K., Keim, B. D., Talbot, R. W., & Mao, H. (2003). Sea breeze: Structure, forecasting, and impacts. *Reviews of Geophysics*, *41*(3). https://doi.org/10.1029/2003RG000124

Mori, S., Jun-Ichi, H., Tauhid, Y. I., Yamanaka, M. D., Okamoto, N., Murata, F., et al. (2004). Diurnal land–sea rainfall peak migration over Sumatera Island, Indonesian Maritime Continent, observed by TRMM satellite and intensive rawinsonde soundings. *Monthly Weather Review*, *132*(8), 2021–2039. https://doi.org/10.1175/1520-0493(2004)132<2021:DLRPMO>2.0.CO;2

Natoli, M. B., & Maloney, E. D. (2019). Intraseasonal variability of the diurnal cycle of precipitation in the Philippines. *Journal of the Atmospheric Sciences*, *76*(11), 3633–3654. https://doi.org/10.1175/JAS-D-19-0152.1

Neale, R., & Slingo, J. (2003). The Maritime Continent and its role in the global climate: A GCM study. *Journal of Climate*, *16*(5), 834–848. https://doi.org/10.1175/1520-0442(2003)016<0834:TMCAIR>2.0.CO;2

Neelin, J. D., Held, I. M., & Cook, K. H. (1987). Evaporation-wind feedback and low-frequency variability in the tropical atmosphere. *Journal of the Atmospheric Sciences*, *44*(16), 2341–2348. https://doi.org/10.1175/1520-0469(1987)044<2341:EWFALF>2.0.CO;2

Neena, J. M., Lee, J. Y., Waliser, D., Wang, B., & Jiang, X. (2014). Predictability of the Madden–Julian Oscillation in the intraseasonal variability hindcast experiment (ISVHE). *Journal of Climate*, *27*(12), 4531–4543. https://doi.org/10.1175/JCLI-D-13-00624.1

Nesbitt, S. W., & Zipser, E. J. (2003). The diurnal cycle of rainfall and convective intensity according to three years of TRMM measurements. *Journal of Climate*, *16*(10), 1456–1475. https://doi.org/10.1175/1520-0442(2003)016<1456:TDCORA>2.0.CO;2

Oh, J. H., Kim, B. M., Kim, K. Y., Song, H. J., & Lim, G. H. (2013). The impact of the diurnal cycle on the MJO over the Maritime Continent: A modeling study assimilating TRMM rain rate into global analysis. *Climate Dynamics*, *40*(3–4), 893–911. https://doi.org/10.1007/s00382-012-1419-8

Oh, J. H., Kim, K. Y., & Lim, G. H. (2012). Impact of MJO on the diurnal cycle of rainfall over the western Maritime Continent in the austral summer. *Climate Dynamics*, *38*(5–6), 1167–1180. https://doi.org/10.1007/s00382-011-1237-4

Peatman, S. C., Matthews, A. J., & Stevens, D. P. (2014). Propagation of the Madden–Julian Oscillation through the Maritime Continent and scale interaction with the diurnal cycle of precipitation. *Quarterly Journal of the Royal Meteorological Society*, *140*(680), 814–825. https://doi.org/10.1002/qj.2161

Peatman, S. C., Matthews, A. J., & Stevens, D. P. (2015). Propagation of the Madden–Julian Oscillation and scale interaction with the diurnal cycle in a high-resolution GCM. *Climate Dynamics*, *45*(9–10), 2901–2918. https://doi.org/10.1007/s00382-015-2513-5

Qian, J. H. (2008). Why precipitation is mostly concentrated over islands in the Maritime Continent. *Journal of the Atmospheric Sciences*, *65*(4), 1428–1441. https://doi.org/10.1175/2007JAS2422.1

Qian, J. H., Robertson, A. W., & Moron, V. (2010). Interactions among ENSO, the monsoon, and diurnal cycle in rainfall variability over Java, Indonesia. *Journal of the Atmospheric Sciences*, *67*(11), 3509–3524. https://doi.org/10.1175/2010JAS3348.1

Qian, J. H., Robertson, A. W., & Moron, V. (2013). Diurnal cycle in different weather regimes and rainfall variability over Borneo associated with ENSO. *Journal of Climate*, *26*(5), 1772–1790. https://doi.org/10.1175/JCLI-D-12-00178.1

Ramage, C. S. (1968). Role of a tropical "maritime continent" in the atmospheric circulation. *Monthly Weather Review*, *96*(6), 365–370. https://doi.org/10.1175/1520-0493(1968)096<0365:ROATMC>2.0.CO;2

Rauniyar, S. P., & Walsh, K. J. (2011). Scale interaction of the diurnal cycle of rainfall over the Maritime Continent and Australia: Influence of the MJO. *Journal of Climate*, *24*(2), 325–348. https://doi.org/10.1175/2010JCLI3673.1

Rauniyar, S. P., & Walsh, K. J. (2013). Influence of ENSO on the diurnal cycle of rainfall over the Maritime Continent and Australia. *Journal of Climate*, *26*(4), 1304–1321. https://doi.org/10.1175/JCLI-D-12-00124.1

Riley Dellaripa, E. M., Maloney, E. D., Toms, B. A., Saleeby, S. M., & van den Heever, S. C. (2019). Topographic effects on the Luzon diurnal cycle during the BSISO. *Journal of the Atmospheric Sciences*, *2019*. https://doi.org/10.1175/JAS-D-19-0046.1

Ruppert, J. H. Jr., Chen, X., & Zhang, F. (2020). Convectively forced diurnal gravity waves in the Maritime Continent. *Journal of the Atmospheric Sciences*, *77*(3), 1119–1136. https://doi.org/10.1175/JAS-D-19-0236.1

Ruppert, J. H. Jr., & Zhang, F. (2019). Diurnal forcing and phase locking of gravity waves in the Maritime Continent. *Journal of the Atmospheric Sciences*, *76*(9), 2815–2835. https://doi.org/10.1175/JAS-D-19-0061.1

Sakaeda, N., Kiladis, G., & Dias, J. (2017). The diurnal cycle of tropical cloudiness and rainfall associated with the Madden–Julian Oscillation. *Journal of Climate*, *30*(11), 3999–4020. https://doi.org/10.1175/JCLI-D-16-0788.1

Seo, K. H., Wang, W., Gottschalck, J., Zhang, Q., Schemm, J. K. E., Higgins, W. R., & Kumar, A. (2009). Evaluation of MJO forecast skill from several statistical and dynamical forecast models. *Journal of Climate*, *22*(9), 2372–2388. https://doi.org/10.1175/2008JCLI2421.1

Short, E., Vincent, C. L., & Lane, T. P. (2019). Diurnal cycle of surface winds in the Maritime Continent observed through satellite scatterometry. *Monthly Weather Review*, *147*(6), 2023–2044. https://doi.org/10.1175/MWR-D-18-0433.1

Simpson, J., Keenan, T. D., Ferrier, B., Simpson, R. H., & Holland, G. J. (1993). Cumulus mergers in the Maritime Continent region. *Meteorology and Atmospheric Physics*, *51*(1–2), 73–99. https://doi.org/10.1007/BF01080881

Skamarock, W. C., Klemp, J. B., Dudhia, J., Gill, D. O., Liu, Z., Berner, J., et al., (2019). A description of the Advanced Research WRF Version 4. *NCAR Technical Notes, NCAR/TN-556+ STR*. http://www2.mmm.ucar.edu/wrf/users/docs/technote/v4_technote.pdf

Sobel, A. H., Maloney, E. D., Bellon, G., & Frierson, D. M. (2008). The role of surface heat fluxes in tropical intraseasonal oscillations. *Nature Geoscience*, *1*(10), 653. https://doi.org/10.1038/ngeo312
Sobel, A. H., Maloney, E. D., Bellon, G., & Frierson, D. M. (2010). Surface fluxes and tropical intraseasonal variability: A reassessment. *Journal of Advances in Modeling Earth Systems*, *2*(1). https://doi.org/10.3894/JAMES.2010.2.2
Straub, K. H. (2013). MJO initiation in the real-time multivariate MJO index. *Journal of Climate*, *26*(4), 1130–1151. https://doi.org/10.1175/JCLI-D-12-00074.1
Sui, C. H., Lau, K. M., Takayabu, Y. N., & Short, D. A. (1997). Diurnal variations in tropical oceanic cumulus convection during TOGA COARE. *Journal of the Atmospheric Sciences*, *54*(5), 639–655. https://doi.org/10.1175/1520-0469(1997)054<0639:DVITOC>2.0.CO;2
Suzuki, T. (2009). Diurnal cycle of deep convection in super clusters embedded in the Madden-Julian Oscillation. *Journal of Geophysical Research*, *114*, D22102. https://doi.org/10.1029/2008JD011303
Taylor, P. C. (2012). Tropical outgoing longwave radiation and longwave cloud forcing diurnal cycles from CERES. *Journal of the Atmospheric Sciences*, *69*(12), 3652–3669. https://doi.org/10.1175/JAS-D-12-088.1
Tian, B., Waliser, D. E., & Fetzer, E. J. (2006). Modulation of the diurnal cycle of tropical deep convective clouds by the MJO. *Geophysical Research Letters*, *33*, L20704. https://doi.org/10.1029/2006GL027752
Vincent, C. L., & Lane, T. P. (2016). Evolution of the diurnal precipitation cycle with the passage of a Madden–Julian Oscillation event through the Maritime Continent. *Monthly Weather Review*, *144*(5), 1983–2005. https://doi.org/10.1175/MWR-D-15-0326.1
Vincent, C. L., & Lane, T. P. (2017). A 10-year austral summer climatology of observed and modeled intraseasonal, mesoscale, and diurnal variations over the Maritime Continent. *Journal of Climate*, *30*(10), 3807–3828. https://doi.org/10.1175/JCLI-D-16-0688.1
Vincent, C. L., & Lane, T. P. (2018). Mesoscale variation in diabatic heating around Sumatra, and its modulation with the Madden–Julian Oscillation. *Monthly Weather Review*, *146*(8), 2599–2614. https://doi.org/10.1175/MWR-D-17-0392.1
Wang, B., & Li, T. (1994). Convective interaction with boundary-layer dynamics in the development of a tropical intraseasonal system. *Journal of the Atmospheric Sciences*, *51*(11), 1386–1400. https://doi.org/10.1175/1520-0469(1994)051<1386:CIWBLD>2.0.CO;2
Wang, S., & Sobel, A. H. (2017). Factors controlling rain on small tropical islands: Diurnal cycle, large-scale wind speed, and topography. *Journal of the Atmospheric Sciences*, *74*(11), 3515–3532. https://doi.org/10.1175/JAS-D-16-0344.1
Wang, S., Sobel, A. H., Tippett, M. K., & Vitart, F. (2019). Prediction and predictability of tropical intraseasonal convection: seasonal dependence and the Maritime Continent prediction barrier. *Climate Dynamics*, *52*(9–10), 6015–6031. https://doi.org/10.1007/s00382-018-4492-9
Wapler, K., & Lane, T. P. (2012). A case of offshore convective initiation by interacting land breezes near Darwin, Australia. *Meteorology and Atmospheric Physics*, *115*(3–4), 123–137. https://doi.org/10.1007/s00703-011-0180-6
Warner, T. T., Mapes, B. E., & Xu, M. (2003). Diurnal patterns of rainfall in northwestern South America. Part II: Model simulations. *Monthly Weather Review*, *131*(5), 813–829. https://doi.org/10.1175/1520-0493(2003)131<0813:DPORIN>2.0.CO;2
Wei, Y., Mu, M., Ren, H. L., & Fu, J. X. (2019). Conditional nonlinear optimal perturbations of moisture triggering primary MJO initiation. *Geophysical Research Letters*, *46*, 3492–3501. https://doi.org/10.1029/2018GL081755
Wei, Y., Ren, H. L., Mu, M., & Fu, J. X. (2020). Nonlinear optimal moisture perturbations as excitation of primary MJO events in a hybrid coupled climate model. *Climate Dynamics*. https://doi.org/10.1007/s00382-019-05021-7
Wheeler, M., & Kiladis, G. N. (1999). Convectively coupled equatorial waves: Analysis of clouds and temperature in the wavenumber–frequency domain. *Journal of the Atmospheric Sciences*, *56*(3), 374–399. https://doi.org/10.1175/1520-0469(1999)056<0374:CCEWAO>2.0.CO;2
Wheeler, M. C., & Hendon, H. H. (2004). An all-season real-time multivariate MJO index: Development of an index for monitoring and prediction. *Monthly Weather Review*, *132*(8), 1917–1932. https://doi.org/10.1175/1520-0493(2004)132<1917:AARMMI>2.0.CO;2
Wu, P., Hara, M., Hamada, J. I., Yamanaka, M. D., & Kimura, F. (2009). Why a large amount of rain falls over the sea in the vicinity of western Sumatra Island during nighttime. *Journal of Applied Meteorology and Climatology*, *48*(7), 1345–1361. https://doi.org/10.1175/2009JAMC2052.1
Xie, Y. B., Chen, S. J., Chang, I. L., & Huang, Y. L. (2018). A preliminarily statistic and synoptic study about the basic currents over southeastern Asia and the initiation of typhoons. *Journal of Meteorological Research*, *32*(4), 661–669. https://doi.org/10.1007/s13351-018-8888-6
Yamanaka, M. D., Ogino, S. Y., Wu, P. M., Jun-Ichi, H., Mori, S., Matsumoto, J., & Syamsudin, F. (2018). Maritime Continent coastlines controlling Earth's climate. *Progress in Earth and Planetary Science*, *5*(1), 21. https://doi.org/10.1186/s40645-018-0174-9
Yanase, A., Yasunaga, K., & Masunaga, H. (2017). Relationship between the direction of diurnal rainfall migration and the ambient wind over the southern Sumatra Island. *Earth and Space Science*, *4*(3), 117–127. https://doi.org/10.1002/2016EA000181
Yang, G. Y., & Slingo, J. (2001). The diurnal cycle in the tropics. *Monthly Weather Review*, *129*(4), 784–801. https://doi.org/10.1175/1520-0493(2001)129<0784:TDCITT>2.0.CO;2
Yokoi, S., Mori, S., Katsumata, M., Geng, B., Yasunaga, K., Syamsudin, F., et al. (2017). Diurnal cycle of precipitation observed in the western coastal area of Sumatra Island: Offshore preconditioning by gravity waves. *Monthly Weather Review*, *145*(9), 3745–3761. https://doi.org/10.1175/MWR-D-16-0468.1
Yokoi, S., Mori, S., Syamsudin, F., Haryoko, U., & Geng, B. (2019). Environmental conditions for nighttime offshore migration of precipitation area as revealed by in situ observation off Sumatra Island. *Monthly Weather Review*, *147*(9), 3391–3407. https://doi.org/10.1175/MWR-D-18-0412.1
Yoneyama, K., & Zhang, C. (2020). Years of the Maritime Continent. https://doi.org/10.1002/essoar.10502015.1
Yu, H., Johnson, R. H., Ciesielski, P. E., & Kuo, H. C. (2018). Observation of quasi-2-day convective disturbances in the equatorial Indian Ocean during DYNAMO. *Journal of the Atmospheric Sciences*, *75*(9), 2867–2888. https://doi.org/10.1175/JAS-D-17-0351.1
Zhang, C. (2005). Madden-Julian Oscillation. *Reviews of Geophysics*, *43*(2). https://doi.org/10.1029/2004RG000158
Zhang, C. (2013). Madden–Julian Oscillation: Bridging weather and climate. *Bulletin of the American Meteorological Society*, *94*(12), 1849–1870. https://doi.org/10.1175/BAMS-D-12-00026.1
Zhang, C., & Ling, J. (2017). Barrier effect of the Indo-Pacific Maritime Continent on the MJO: Perspectives from tracking MJO precipitation. *Journal of Climate*, *30*(9), 3439–3459. https://doi.org/10.1175/JCLI-D-16-0614.1